MINISTRY OF EDUCATION AND TRAINING

HANOI NATIONAL UNIVERSITY OF EDUCATION

DAO VIET THANG

SYNTHESIS $BiFeO_3$, DOPED-$BiFeO_3$ MATERIALS AND STUDY SOME OF THEIR PROPERTIES

Specialization: Solid State Physics

Code: 62.44.01.04

ABSTRACT OF PHYSICS DOCTORAL THESIS

Hanoi – 2017

This work has been completed at:

The Faculty of physics and Center for Nano Science and Technology,

Hanoi National University of Education

Scientific instructor:

1. **Assoc. Prof. Dr. Du Thi Xuan Thao**
2. **Prof. Dr. Nguyen Van Minh**

Reviewer 1: Assoc. Prof. Dr. Nguyen Van Nha

Nguyen Trai University

Reviewer 2: Assoc. Prof. Dr. Le Thi Thanh Binh

Hanoi University of Science, Vietnam National University

Reviewer 3: Assoc. Prof. Pham Van Hoi

Institute of Materials Science, Vietnam Academy of Science and Technology

The thesis will be defended before the Council for evaluation thesis at Hanoi National University of Education at .....hours.... days ..... year 2017.

Thesis can be found at the library:

- *Library of National, Hanoi.*
- *Library of Hanoi National University of Education.*

INTRODUCTION

Multiferroics present two or more than two ferroic properties such as ferroelectric, ferroelastic, ferromagnetic, and antiferromagnetic in the same phase. Interaction between different orders in multiferroics is usually exhibited in magnetoelectric effect which is considered as a coupling between spontaneous polarization *Ps* and spontaneous magnetization *Ms*. Therefore, multiferroics can be magnetized under an external electric field or polarized under an external magnetic field. Multiferroics are good candidates for producing high techonology devices such as computer memory, sensors and spintronic device.

$BiFeO_3$ is one of a few materials which exhibits simultaneously ferroelectric order and antiferromagnetic order in the same phase. $BiFeO_3$ material shows ferroelectric properties with large spontaneous polarization and dielectric constant below Curie temperature T_C = 1100 K. $BiFeO_3$ exhibits antiferromagnetic property below Néel temperature T_N = 643 K. Moreover, it possesses a small band gap energy of E_g = 1.3 ÷ 2.8 eV for bulk, E_g = 2.5 ÷ 3.1 eV for thin film and E_g = 2.1 eV for powder.

$BiFeO_3$ is restricted in application due to its room temperature spontaneous magnetization is quite small. Allmost reported studies concentrated on improving ferroic properties of $BiFeO_3$ in some different routes as follow: (i) substituting or co-substituting rare-earth ions such as Nd^{3+}, Gd^{3+}, Ho^{3+}, Y^{3+}, Sm^{3+}, La^{3+} and Eu^{3+} into Bi-site and transition metal ions such as Mn^{2+}, Ni^{2+}, Co^{2+}, Cu^{2+} into Fe-site; (ii) creating composite materials between $BiFeO_3$ with other materials to induce magnetoelectric effect through elastic interactions between two phases.

For studies based on $BiFeO_3$, it is very important to find out experimental condition to successfully fabricate single-phase crystals of both pure $BiFeO_3$ and doped-$BiFeO_3$. In addition, it is also very necessary to find out the relationship between rare-earth and transition metal doping to the change in physical properties, especially magnetic property. The results will be contributed to general understanding and also to future application of $BiFeO_3$. For these reasons, we have chosen the title of thesis as: "***Synthesis $BiFeO_3$, doped-$BiFeO_3$ materials and study some of their properties***"

The objective of the thesis: (i) Fabricating $BiFeO_3$ by different methods and technologies. Investigating the influence of fabrication conditions on crystal structure, crystal lattice vibrations, magnetic and optical properties of $BiFeO_3$ using different measurements; (ii) Investigating the influence of rare-earth doping on crystal structure, crystal lattice vibrations, electromagnetic and optical properties of $BiFeO_3$; (iii) Investigating the improvement ferroelectric and ferromagnetic properties of $BiFeO_3$ co-doped with rare-earth and transition metal ions. Researching the influence of impurities concentration on crystal structure, crystal lattice vibrations, ferromagnetic, ferroelectric and optical properties of $BiFeO_3$ to find out which concentration is suitable for the improvement of ferroic properties of materials.

Study subjects:

- $BiFeO_3$.
- Rare-earth doped $BiFeO_3$ with rare earth ions of (Nd^{3+}, Gd^{3+}, Sm^{3+}, Y^{3+}).
- Rare-earth and transition metal co-doped $BiFeO_3$.

Research methods: Thesis was studied using primaly experimental methods. In addition, some analysing softwares were used to investigate the effects of technology conditions and the influence of doping of rare-earth and co-doping of rare-earth and trasition metal on the physical properties of

$BiFeO_3$. The crystal tructure, and surface morphology of samples were analyzed using modern measurements as X-ray diffraction (XRD), scanning electron microscopy (SEM), transmission electronmicroscopy (TEM) images. The influence of rare-earth and transition metal ionics to crystal lattice vibrations was determined by Raman spectroscopic measurements.The optical properties were analyzed using absorption spectroscopic measurements. The magnetic properties were analyzed using magnetization hysteresis (*M* - *H*) loops measurements. Electrical properties were determined by impedance spectroscopy and polarization hysteresis loops measurements. The measurements were carried out by modern equipmentswith high reliability at national research centers, a few measurements were done in foreign laboratories.

Scientific meaning and practical significance of the thesis: The major purpose of thesis is improving ferroic properties of $BiFeO_3$. The research results reflecte the impact of technological conditions on phase formation of $BiFeO_3$ and hence the optimise process for manufacturing $BiFeO_3$. In addition, the thesis also reveals the influence of doping of rare-earth and co-doping of rae earth and transition metal on crystal struture, crystal lattice vibrations, optical, electrical, and magnetic properties of the materials. These results will contribute to the understanding of $BiFeO_3$ in terms of basic and application-oriented research.

The contents of the thesis include: (i) general introduction of multiferroic materials, structural and physical characterations of $BiFeO_3$, and some previous studies on doped and un-doped $BiFeO_3$; (ii) experimental techniques; and (iii) major results of the influence of experimental conditions on $BiFeO_3$ fabrication, the influence of doping of rare-earth and co-doping of rare-earth and transition metal on crystal structure, crystal lattice vibrations, optical, electrical and magnetic properties of $BiFeO_3$.

The layout of the thesis: Thesis is presented in 149 pages with 106 Figures and 35 Tables, including the heading, 5 chapters, conclusion, a list of publications, and references. Structure of the thesis as follows:

Heading: Introducing research situation and the necessary of the thesis; the physical meaning, the content and the structure of the thesis.

Chapter 1: Overview of multiferroic materials and $BiFeO_3$; some previous studies on improving ferroic properties of $BiFeO_3$ material.

Chapter 2: Experimental methods and processes to synthesize materials, basic principles of expermental measurements used to analyze crystal structure and physical properties of materials.

Chapter 3: Presenting the influence of technological conditions to crystal structure, and physical properties of $BiFeO_3$.

Chapter 4: Presenting the effect of doping of rare-earth (R^{3+} = Nd^{3+}, Gd^{3+}, Sm^{3+}, and Y^{3+}) on crystal structure and physical properties of $BiFeO_3$.

Chapter 5: Presenting the influence of co-doping of rare-earth Nd^{3+}(or Gd^{3+}) and transition metal (Ni^{2+}) on crystal struture and physical properties of $BiFeO_3$. Conclusion: Presenting the major results of the thesis.

The research results of the thesis have been published in 16 scientific works in which there are 6 articles in national journals, 4 reports in national and international conferences, 3 articles in international journals, and 3 scientific works related to content research.

Chapter 1: OVERVIEW OF MULTIFERROIC MATERIALS AND $BiFeO_3$

1.1. ABO_3 materials

1.1.1. Crystal structure and crystal lattice distortion

1.1.1.1. Perovskite structure

The ideal ABO_3 perovskite structure is cubic in which cation *B* locates at the center of the cube, cations *A* locate at 8 peaks of the cube, and anions O locate at the face center of the cube. An important characteristic of the perovskite structure is the existence of octahedral BO_6 with 6 anions O located at 6 peaks of the octahedral and cation *B* located at the center of the octahedral.

1.1.1.2. The energy splitting in octahedral crystal field

In octahedral BO_6, electrostatic interactions between cations *B* and anions O lead to the splitting of energy levels. Electronic-magnetic properties of materials depend on the arrangement of electrons in orbitals *d* of cation *B*. Under the effect of octahedral field, energy of orbitals *d* of transition metal is separated into different energy levels, symbolled as t_{2g} and e_g.

1.1.1.3. Effects Jahn - Teller and the crystal lattice distortion

In Jahn - Teller theory, when structure is symmetrical and electron orbital is degraded, the structure will be deformed to remove the degeneracy. This process results in reducing symmetry and reduced free energy. Jahn - Teller (JT) effects occurs in metal ionic that contains an odd number electronics on e_g energy level.

1.1.2. Some mechanisms to explain magnetic properties of perovskite structure

1.2. Multiferroic materials

1.2.1. History of multiferroic study

1.2.2. Physical properties of the multiferroic materials

Multiferroic materials with the existence of ferroic properties in the same phase show magneto-electric effects which is a promising property for fabrication of new materials. Typical multiferroic materials belong to the group of the perovskite transition metal oxides, and include rare-earth magnetites and ferrites ($TbMnO_3$, $HoMn_2O_5$ and $LuFe_2O_4$). Other examples are bismuth alloys $BiFeO_3$ and $BiMnO_3$, and non-oxides such as $BaNiF_4$.

1.2.2.1. Ferroelectric properties

Ferroelectric properties of the materialsare are characterized by polarization hysteresis loops. It is derived from: (i) Perovskite types multiferroic; (ii) Ferroelectricity due to lone pairs; (iii) Ferroelectricity due to charge ordering.

1.2.2.2. Ferromagnetic and antiferromagnetic properties

Ferromagnetism is existence of a spontaneous magnetisation which can be reversed by an opposite magnetic field, and is perfectly analogous to ferroelectricity. Ferromagnetic moments arise from ordering of spins of unpaired electrons on *d* or *f* of orbitals. Ferromagnetism become paramagnetic above ferromagnetic Curie temperature T_C of the materials. In perovskites ferromagnetic superexchange can take place between the e_g of 3*d* orbitals of metals through 2*p* orbitals of O or between half-filled and empty e_g orbitals.

Antiferromagnetism becomes paramagnetic above Néel temperature T_N, where the magnetic susceptibility passes through a maximum, as the sublattice antiparallel to the magnetic field is most susceptible to reorientation by a field at T_N. The spins on cations *B* couple through anions oxygen by a virtual electron transfer mechanism known as superexchange. Intra-atomic interactions cause the

spins on each cation *B* to align parallel, which are obeyed Hund's rule. Degeneracy of the *d* orbitals is lifted in an octahedral crystals field. Superexchange between e_g orbitals (σ-interactions) is stronger than superexchange between t_{2g} orbitals (π-interactions).

1.2.2.3. Magnetoelectric effect (ME) in multiferroic materials

In multiferroics, coupling between (anti-) ferroelectricity and (anti-) ferromagnetism will lead to ME effect in which magnetic (electric) polarization will be induced by applying an external electric (magnetic) field. The effect can be linear or/and non-linear with respect to the external fields. The effect can be obtained from differentiation of expansion of free energy of materials leading to the polarization in direction can be represented by expressions (1.6)

$$F(E,H) = F_0 - P_i^s E_i - M_i^s H_i - \frac{1}{2}\varepsilon_0 \varepsilon_{ij} E_i E_j - \frac{1}{2}\mu_0 \mu_{ij} H_i H_j - \alpha_{ij} E_i H_j - \frac{1}{2}\beta_{ijk} E_i H_j H_k - \frac{1}{2}\gamma_{ijk} H_i E_j E_k - ..., \quad (1.6)$$

1.3. $BiFeO_3$ materials

1.3.1. Crystal structure of $BiFeO_3$

$BiFeO_3$ (BFO) can exist in different types of crystal structures. The crystal structure of BFO is a rhombohedrally distorted perovskite with space group *R3c* or $R\bar{3}c$, or orthorhombic structure with space group *Pnma*, monoclinic structure with space group *Cm* or tetragonal perovskites with space group *P4mm* and cubic structure with space group $Fm\bar{3}m$. Normally, BFO exists in rhombohedral structure (lattice parameters a = 5.579 Å and c = 13.869 Å).

1.3.2. Crystal lattice vibrations of $BiFeO_3$

In the rhombohedral structure, BFO has 13 Raman modes ($4A_1$ + $9E$). Mode A_1 and E at wavenumber lower than 400 cm^{-1} characterize for Bi-O covalent bonds. At above wavenumber of 400 cm^{-1}, mode E characterize for Fe-O covalent bond vibrations. Raman spectrum of BFO has wide spectrum at the wavenumber 1000 ÷ 1300 cm^{-1}. It is contributed by three peaks $2A_4$ (~ 960 cm^{-1}), $2E_8$ (~ 1110 cm^{-1}), $2E_9$ (~ 1260 cm^{-1}). The peak $2A_4$ is overtone of Bi-O vibration, the peak $2E_8$ is overtone of Fe-O_1 bonding vibration and the $2E_9$ is of Fe-O_2, where O_1 are axial and O_2 are equatorial ions.

1.3.3. Electrical properties of $BiFeO_3$

1.3.4. Ferroelectric properties of $BiFeO_3$

$BiFeO_3$ is a rhombohedral distorted ferroelectric with space group *R3c* and Curie temperature of Tc = 1100 K. The popularity of bismuth ferrite, in which stereochemical activity of the Bi lone electron pair gives rise to ferroelectric polarization. Saturated electric polarization of $BiFeO_3$ depends on type of $BiFeO_3$. The experimental results showed that samples are often polycrystalline with large leakage current density which leads to a small electric polarization.

1.3.5. Magnetic properties of $BiFeO_3$

$BiFeO_3$ is antiferromagnetic with G-type ordering, in analogy with rock salt crystal structure; each Fe^{3+} with spin up is surrounded by six nearest neighbours with spin down. $BiFeO_3$ crystallites exhibit strong antiferromagnetic (G–type spin structure, T_N = 643 K). Magnetic properties in $BiFeO_3$ originates from the half filled and localized $(t_{2g}^3 e_g^2)$ Fe^{3+} cations. In addition, magnetic order still exists at temperatures of 140 and 200 K. Magnetic properties are derived from superexchange interactions and Dzyaloshinskii-Moriya (D - M) interactions.

1.3.6. Optical properties of $BiFeO_3$

$BiFeO_3$ is a semiconductor with narrow band gap. Optical band gap (E_g) of $BiFeO_3$ is about 1.3 ÷ 2.8 eV. If electronics transfer is indirect, E_g = 1.3 ÷ 1.8 eV. Conversely, if electronics transfer is direct, E_g = 2.17 ÷ 2.81 eV. These experimental results are quite consistent with the theoretical values

(E_g = 1.9 ÷ 2.8 eV). The top of valence bands is predominantly formed by O-p states and minorly contributed by Bi-p and Fe-*d* states. At the bottom of conduction band, Fe-*d* states contribute primaly and O-*p* states provide only a little. The middle conduction bands are occupied dominantly by Bi-*p*, Fe-*s* states.

1.4. Rare-earth doped $BiFeO_3$

1.4.1. Crystals structure and crystal lattice vibrations

Experimental data showed that doping with rare-earth ionics such as Y^{3+}, La^{3+}, Nd^{3+}, Sm^{3+}, Gd^{3+}, and Ho^{3+} leaded to a decreasing of lattice constants, particle size, and crystal lattice volume of $BiFeO_3$ crystallites. Effect of rare-earth ionic is demonstrated by Raman scattering spectra. Namely the modes characterized for Bi-O bonding, the peaks are shifted toward higher wavenumber along with a decrease in intensity when doping concentration of rare-earth increase. In Nd^{3+}doped $BiFeO_3$, modes *E-1*, A_1-1, A_1-2, A_1-3, A_1-4, and *E*-2 are shifted toward a higher wavenumber. Other rare-earth ionics have a similar results. In addition, a structural phase transition occurs at high doping concentration.

1.4.2. Magnetic properties in rare-earth doped $BiFeO_3$

Ms and *Mr* increase significantly in rare-earth doped $BiFeO_3$ (Table 1.7).

Table 1.7. *Ms* and *Mr of* rare-earth doped $BiFeO_3$

Contents	Ho^{3+}(*H* = 30 kOe)		Y^{3+} (*H* = 20 kOe)		La^{3+}(*H* = 55 kOe)		Nd^{3+}(*H* = 5 kOe)	
	Mr (emu/g)	*Ms* (emu/g)	*Mr* (emu/g)	*Ms* (emu/g)	*Mr* (emu/g)	*Ms* (emu/g)	*Mr* (emu/g)	*Ms* (emu/g)
0.00	0.0024	0.20195	---	- - -	0.0038	0.35	- - -	- - -
0.05	0.0075	0.49691	0.0264	0.7468	0.0032	0.35	0.0059	- - -
0.10	0.0840	0.93133	0.0545	2.1108	0.0077	0.40	0.0153	- - -
0.15	0.1146	1.05938	0.1019	3.3276	0.0215	0.40	0.0440	- - -
0.20	0.1167	1.28064	0.1165	6.2703	0.0736	0.55	- - -	- - -

1.4.3. Ferroelectric properties in rare-earth doped $BiFeO_3$

In Gd^{3+}(or Nd^{3+}) doped $BiFeO_3$, *Ps* and *Pr* increase with the concentrations of Gd^{3+} (or Nd^{3+}). When concentrations of Nd^{3+} is 10 and 17.5 mol%, *Pr* and *Ps* are 9 and 19 μC/cm^2, respectively. When the concentrations of Nd^{3+} increase to 20 mol%, ferroelectric materials transition to paraelectric materials with *Pr* = 0.19 μC/cm^2.

1.5. Transition metal doped $BiFeO_3$

Compare to undoped $BiFeO_3$, transition metal (Ni^{2+} or Mn^{3+}) doped $BiFeO_3$ has some changes in crystal structure, electrical, magnetic and optical properties. X-ray diffraction diagram of Mn^{3+} doped $BiFeO_3$ shows rhombohedral structure. In addition, when concentrations of Mn^{3+} is larger than 5 mol%, a structural phase transitions are observed in both the XRD diagram and Raman scattering spectroscopy. In case of Ni^{2+} doped $BiFeO_3$, lattice constants and crystal lattice volume are decrease. Ni^{2+} doped $BiFeO_3$ often appears $Bi_2Fe_4O_9$, $Bi_{25}FeO_{40}$ phases. Transition metal doped $BiFeO_3$ showed some improved ferromagnetic properties. However, the ferroelectric properties of these materials did not be improved much.

1.6. Rare-earth and transition metal co-doped $BiFeO_3$

Recent studies showed that ferroelectric and ferromagnetic properties of $BiFeO_3$ were improved by co-doping of rare-earth and transition metal ionics. The ferroelectric and ferromagnetic properties

of $BiFeO_3$ were improved when co-doping (Ho^{3+}, Mn^{3+}). The results were similar when co-doping (Sm^{3+}, Mn^{3+}) or (Dy^{3+}, Mn^{3+}).

Chapter 2: FABRICATION METHODS AND ANALYSIS PROPERTIES MEASUREMENTS OF MATERIALS

2.1. Fabrication methods

The samples were prepared by solid state reaction, hydrothermal, and sol - gel methods.

2.1.4. The symbols of samples in the thesis

Table 2.1. Symbols of samples used to study in the thesis

1	The $BiFeO_3$ samples were prepared by three methods						
	Solid state reaction		Hydrothermal		Sol - gel		
	SS		HT		SG		
2	The $BiFeO_3$ samples were prepared by hydrothermal method with different concentrations of KOH						
	4 M	5 M	6 M		7 M	8 M	
	HC4	HC5	HC6		HC7	HC8	
3	The $BiFeO_3$ samples were prepared by hydrothermal method with different hydrothermal times						
	2 hours	4 hours	6 hours	8 hours	10 hours	12 hours	
	H2	H4	H6	H8	H10	H12	
4	The $BiFeO_3$ samples were prepared by sol - gel method with different annealing temperature						
	500 °C	600 °C	700 °C	800 °C	850 °C		
	S500	S600	S700	S800	S850		
5	The rare-earth doped $BiFeO_3$ were prepared by sol - gel method						
	Symbol	*x* / *RE*	2.5 %	5%	7.5%	10%	12.5%	15%
	SNd	Nd	SNd2.5	SNd5	SNd7.5	SNd10	SNd12.5	SNd15
	SGd	Gd	SGd2.5	SGd5	SGd7.5	SGd10	SGd12.5	SGd15
			5 %	10 %	15 %	20 %		
	SSm	Sm	SSm5	SSm10	SSm15	SSm20		
	SY	Y	SY5	SY10	SY15	SY20		
6	The $Bi_{1-x}RE_xFe_{0.975}Ni_{0.025}O_3$ (*RE* = Nd, Gd) sampels were prepared by sol - gel method						
	Symbol	*x* / *RE*	2.5%	5%	7.5%	10%	12.5%	15%
	SNiNd	Nd	NiNd2,5	NiNd5	NiNd7,5	NiNd10	NiNd12,5	NiNd15
	SNiGd	Gd	NiGd2,5	NiGd5	NiGd7,5	NiGd10	NiGd12,5	NiGd15
	$Bi_{1-x}RE_xFe_{0.975}Ni_{0.025}O_3$ (*RE* = Nd, Gd) sample with x = 0% was denoted by BFNO $Bi_{0.90}Nd_{0.10}Fe_{0.95}Ni_{0.05}O_3$ sample was denoted by BNFNO						

2.2. Measurement techniques and analysis properties measurements of materials

Measurements techniques and physical properties analysis of materials are DTA and TGA; X-ray diffraction patterns; Raman scattering spectroscopy; EDS; SEM; TEM; optical absorption spectroscopy; Magnetic hysteresis loops; impedance spectrum, and $P - E$ hysteresis loops.

Chapter 3: CRYSTAL STRUCTURE AND PHYSICAL PROPERTIES OF $BiFeO_3$ SYNTHESIZED BY DIFFERENT METHODES

3.1. Crystal structure, crystal lattice vibrations and surface morphology of $BiFeO_3$ synthesized by different methods

3.1.1. Crystal structure of $BiFeO_3$

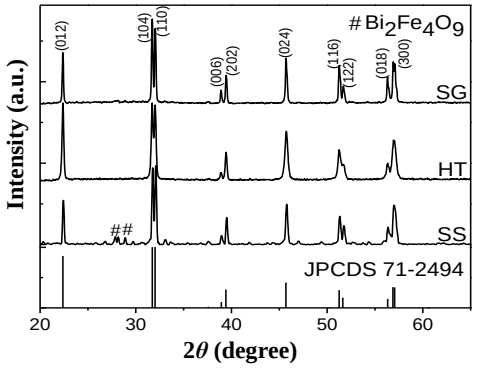

Fig.3.1. X-ray diffraction patterns of $BiFeO_3$ prepared by solid-state (SS), hydrothermal (HT) and sol-gel (SG) process.

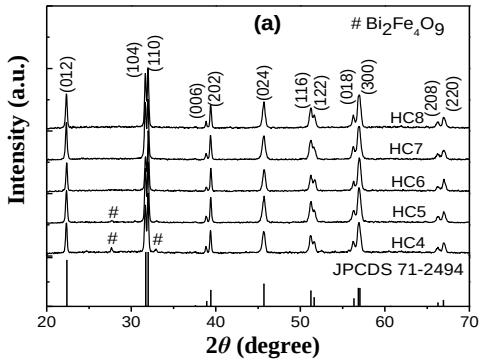

Fig. 3.2. X-ray diffraction patterns of HC4, HC5, HC6, HC7, and HC8 samples

Fig. 3.1 shows X-ray diffraction (XRD) patterns of $BiFeO_3$ prepared by different methods. All XRD peaks are consistent with JPCDS card No. 71-2494 of crystal $BiFeO_3$. According to this card, $BiFeO_3$ have rhombohedral distorted perovskite structure with space group *R3c* and lattice parameters $a = b = 5.587$ Å, and $c = 13.867$ Å. In addition, X-ray diffraction pattern of SS sample shows an appearance of the peaks at 2θ angle around 27.96 and 28.91°. These peaks characterize for $Bi_2Fe_4O_9$ phase according to JPCDS card No. 72-1832. Fig. 3.2 shows XRD of HC4, HC5, HC6, HC7, and HC8 samples which shows a single-phase structure of HC6, HC7, and HC8 samples. Figure 3.3a also shows that H4, H6, H8, H10 and H12 samples crystalline in single-phase structure while H2 sample is not single-phase structure.

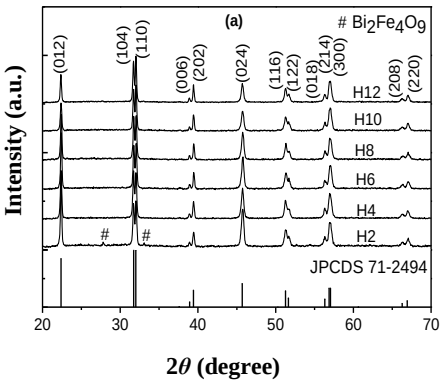

Fig.3.3. (a) X-ray diffraction diagram of H2, H4, H6, H8, H10, and H12 samples.

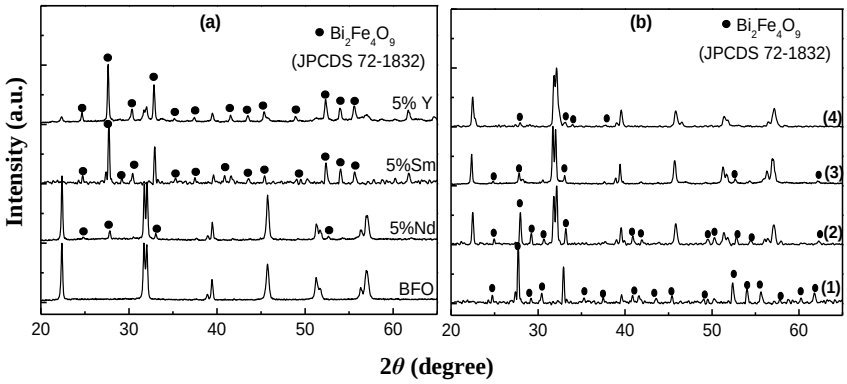

Fig. 3.4. (a) X-ray diffraction diagram of $Bi_{0.95}RE_{0.05}FeO_3$ (RE = Nd, Sm, Y); (b) X-ray diffraction diagram of $Bi_{0.95}Sm_{0.05}FeO_3$, (1) Not annealed, (2) annealed at 600 °C, (3) annealed at 700 °C, (4) annealed at 800 °C

Figure 3.4 shows XRD patterns of rare-earth doped $BiFeO_3$ prepared by hydrothermal method. These samples are not single-phase revealed by the presence of many impurity XRD peakes

For sol-gel method, differential thermal (DTA) and thermal mass (TGA) curves of $BiFeO_3$ gels are showed in Fig. 3.5. An exothermal peak at temperature 430 °C observed in DTA curve agrees well with TGA result where the mass of the sample keeps constantly above 430 °C. Therefore, crystalline BFO phase is predicted forming at temperature about 430 °C. Then, annealing temperatures are selected of 500, 600, 700, 800, and 850 °C.

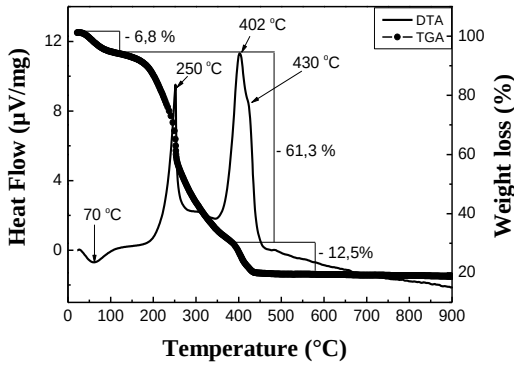

Fig. 3.5. DTA and TGA curves of $BiFeO_3$ gels

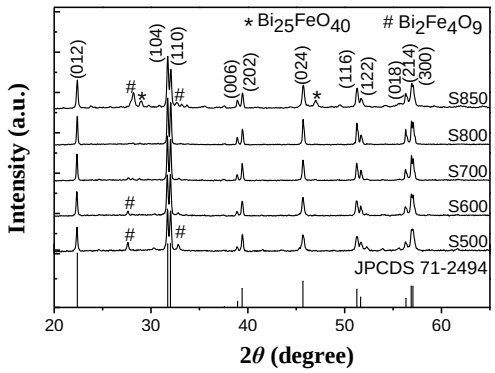

Fig. 3.6. X-ray diffraction diagram of S500, S700, S800, and S850 samples

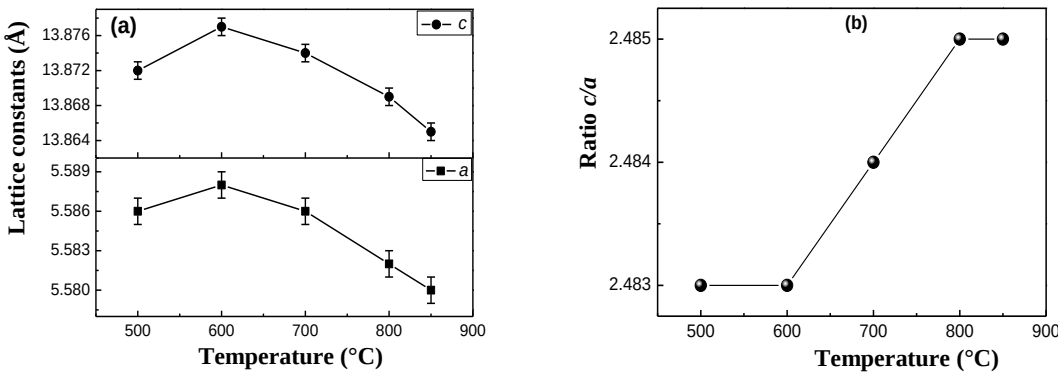

Fig. 3.7. (a) Lattice constants and (b) ratio c/a change according annealing temperature samples

Figure 3.6 shows X-ray diffraction patterns of $BiFeO_3$ samples annealed at different temperatures. All XRD peaks are consistent with card JPCDS No. 71 - 2494. The XRD results show that only S800 sample is formed in single-phase structure. Lattice constants of the samples were determined by UnitCell software. It shows that the lattice constants of $BiFeO_3$ change when the annealing temperature change (Fig. 3.7).

3.1.2. Crystal lattice vibrations of $BiFeO_3$

Raman scattering spectra of SS, HT, and SG samples measured at room temperature showed in Fig. 3.8 are consistent with previous studies. Modes A_1, E-2 and E-3 are characterized for Bi - O covalent bonds, and modes E are characterized for Fe - O covalent bonds.

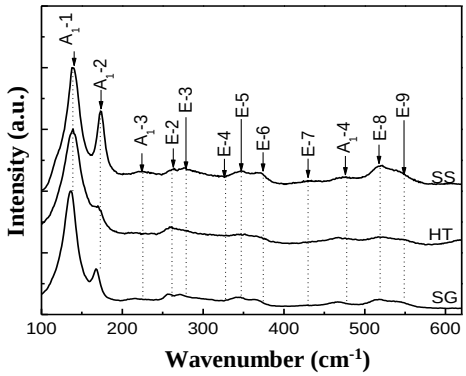

Fig. 3.8. Raman scattering spectra of $BiFeO_3$ were prepared by different methods

Fig. 3.9a shows Raman scattering spectra of $BiFeO_3$ measured at temperature range from 13 to 280 K. Raman scattering spectra of $BiFeO_3$ contain wide spectral regions at wavenumber range 1000 ÷ 1400 cm^{-1} with a strong intensity. The origin of these band has been assigned to a combination of three different two-phonon

Raman overtones labeled $2A_1$-4, $2E$-8 and $2E$-9. The modes $2A_1$-4, $2E$-8 and $2E$-9 are overtone of Bi - O, Fe - O_1, Fe - O_2 bonding vibrations, respectively. Fig. 3.10a shows that $2A_1$-4 and $2E$-8 peaks shift gently toward higher wavenumber when temperature increases from 13 to 280 K. The position of $2E$-9 peak shifts toward higher wavenumber as temperature increases from 13 to 180 K and shifts toward lower wavenumber when temperature ≥ 230 K. The intensity of $2A_1$-4, $2E$-8, and $2E$-9 peaks as well as the ratio of peak intensity $2E$-8/$2E$-9 decreases sharply at temperature 230 K (Fig. 3.10b).

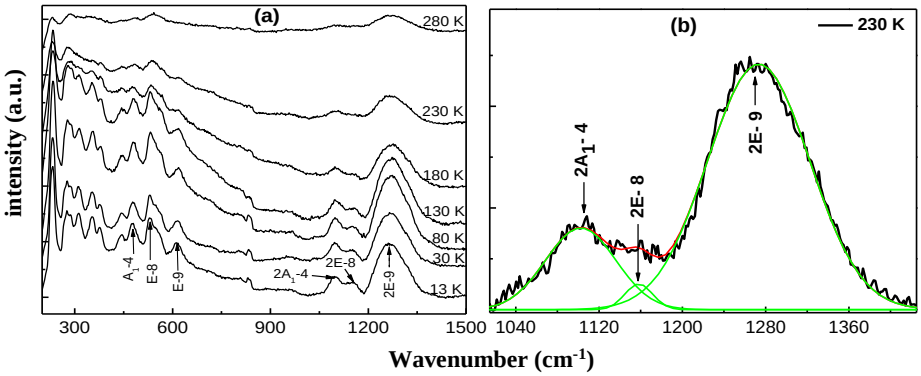

Fig. 3.9. (a) Raman scattering spectra of $BiFeO_3$ at temperature low (b) The peaks $2A_1$-4, 2E-8, and 2E-9 of the samples measured at 230 K were fitted by Gaussian function

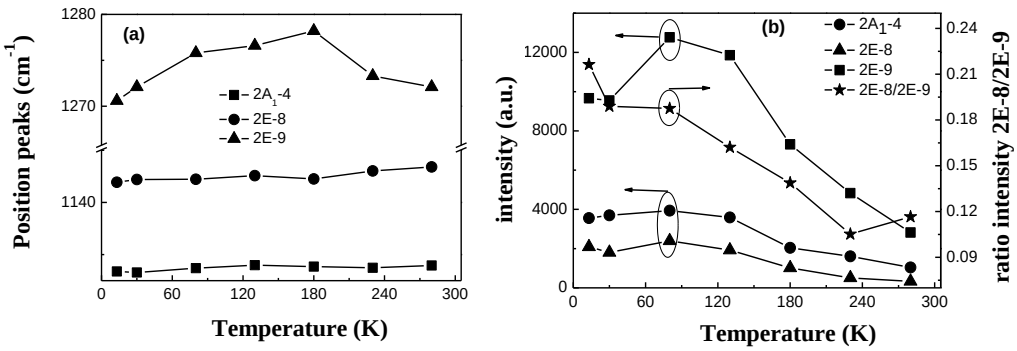

Fig. 3.10. (a) Position peaks $2A_1$-4, 2E-8, 2E-9 and (b) Intensity peaks $2A_1$-4, 2E-8, 2E-9 and ratio intensity of peaks 2E-8/2E-9 depends the temperature

Fig. 3.11 shows Raman scattering spectra of S500, S600, S700, S800 and S850 samples. Peaks A_1-1, A_1-2 shifted toward a higher wavenumber when annealing temperature increased from 500 to 850 °C. Peak A_1-3 also shifted toward the higher wavenumber when annealing temperature increased from 500 to 700 °C and shifted toward lower wavenumber when annealing temperature increased from 800 to 850 °C. Peaks E-8, E-9 with peak shifted with the opposed rule compared to A_1-3. A small peak at wavenumber 225 cm^{-1} appears in Raman scattering spectra of S500, S600, S700 and S850 samples. We anticipated that this peak is related to the presence of $Bi_2Fe_4O_9$ phase because it is not observed in Raman scattering spectrum of S800 sample.

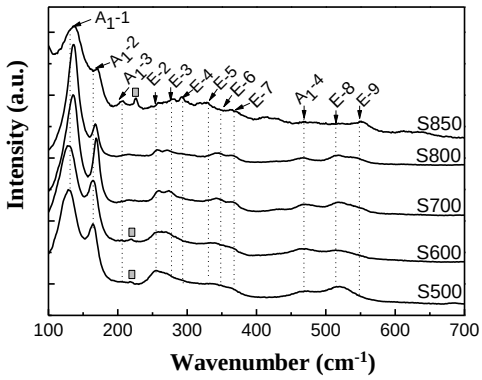

Fig. 3.11. (a) Raman scattering spectra of S500, S600, S700, S800 and S850 samples

3.1.3. The surface of morphology of $BiFeO_3$

3.2. Physical properties of $BiFeO_3$, samples were manufactured in different conditions

3.2.1. Magnetic properties of $BiFeO_3$

Magnetic properties of $BiFeO_3$ were surveyed by magnetic hysteresis loops. Figure 3.14a shows magnetic hysteresis loops of $BiFeO_3$ synthesized at different hydrothermal time. The results show that all samples have a weak ferromagnetic properties. Figure 3.14b shows the *Ms* values of H2, H4, H6, H8, H10, and H12 samples. Due to the contribution of $Bi_2Fe_4O_9$ phase, the H2 sample exhibits a larger *Ms* value than that of different samples. For single-phase structure samples, *Ms* decreased when hydrothermal time increased.

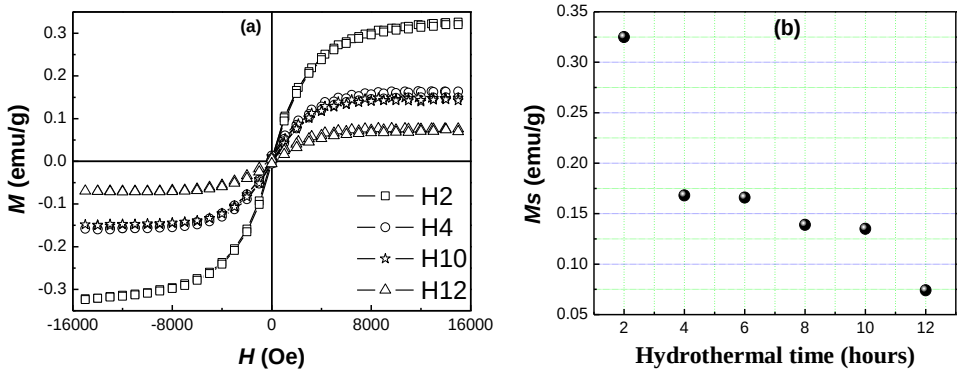

Fig. 3.14. (a) Magnetic hysteresis loops of H2, H4, H10 and H12 samples; (b) Ms value of $BiFeO_3$ changes according hydrothermal time

Figure 3.15a shows magnetic hysteresis loops of S500, S600, S700, and S800 samples measured at room temperature with maximum magnetic field of 10 kOe. *Ms* and *Mr* values change according annealing temperature as show in Fig. 3.15b. We could see that all the samples showed weak ferromagnetic properties. *Ms* and *Mr* values decreased sharply when annealing temperature increased from 500 to 700 °C, and they change minorly when annealing temperature increased from 700 to 800 °C.

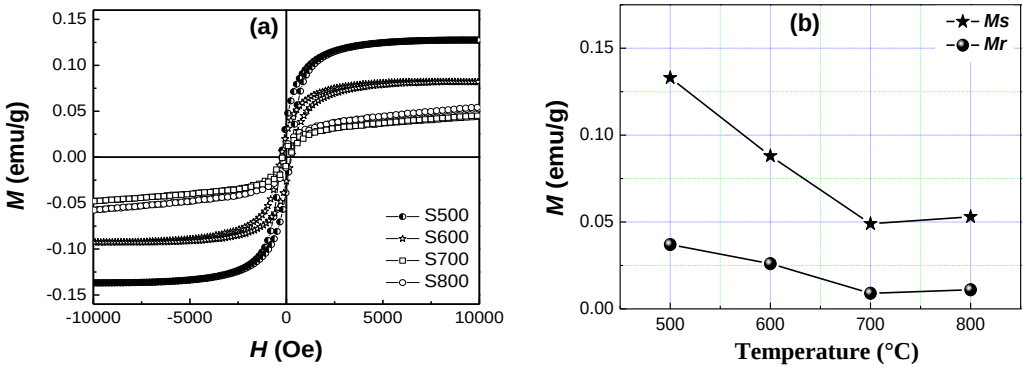

Fig. 3.15. (a) Magnetic hysteresis loops and (b) Ms and Mr values of S500, S600, S700 and

From the above results, we can conclude that sol-gel is the most suitable process to synthesize single-phase $BiFeO_3$ crystallites and the optimize condition is annealing temperature of 800 °C and annealing time of 7 hours. $BiFeO_3$ prepared by sol-gel method exhibits a weak ferromagnetic order with *Ms* = 0.053 emu/g, and *Mr* = 0.011 emu/g.

3.2.2. Optical properties of $BiFeO_3$

Optical properties of $BiFeO_3$ were assessed through UV-vis absorption spectroscopy. Figure 3.16a shows absorption spectra of $BiFeO_3$ synthesized at different hydrothermal time. It is obvious that all samples have an abdorption peak at wavelength of 500 nm, absorption edge at wavelength about 500 ÷ 600 nm which are assigned to electronic transfer from O-2p states in valence band to Fe-3d states in conduction band. The second absorption edge at wavelength about 650 ÷ 750 nm are attributed to electronic transfer from t_{2g} to e_g energy levels of Fe-d orbitals. Therefore, the optical band gap of $BiFeO_3$ can be identified for the first absorption edge. Fig. 3.16b shows how determine E_g of H2, E_g of remaining samples are determine similarly. We observed that optical band gap of the H2, H4, H6, H8, H10, and H12 samples changed in the range 2.08 ÷ 2.03 eV when hydrothermal time changed from 2 to 12 hours.

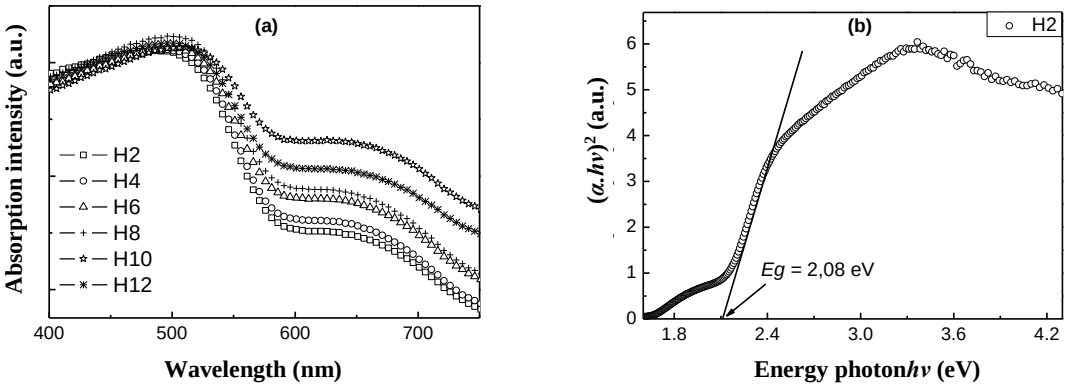

Fig. 3.16. (a) Absorption spectroscopy of H2, H4, H6, H8, H10 and H12 samples; (b) Performances $(\alpha.h\nu)^2$ change versus energy photon ($h\nu$) of H2 sample

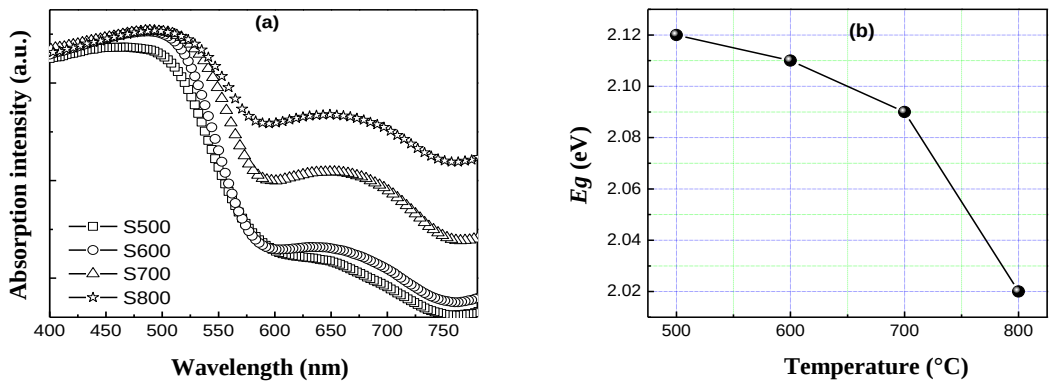

Fig. 3.18. (a) Absorption spectroscopy and (b) E_g values of S500, S600, S700, and S800 samples

Effect of annealing temperature on optical properties of $BiFeO_3$ is determined by UV-Vis absorption spectroscopy. The results obtained show that the optical band gap of this material decreased from 2.12 to 2.05 eV as the annealing temperature increased from 500 to 800 °C (Fig. 3.18b).

As mentioned above, $BiFeO_3$ was manufactured sol-gel method and annealed temperature at 800 °C for 7 hours was the best condition. $BiFeO_3$ was manufactured in these conditions that has optical band gap of about 2.02 eV. This was the basis when studied optical properties of doped-$BiFeO_3$.

Chapter 4: CRYSTAL STRUCTURE, PHYSICAL PROPERTIES OF RARE-EARTH IONICS DOPED $BiFeO_3$

4.1. Crystal structure, crystal lattice vibrations and surface morphology of $Bi_{1-x}RE_xFeO_3$ (*RE* = Nd, Gd, Sm, Y; *x* = 0.00 ÷ 0.20)

4.1.1. Crystal structure of $Bi_{1-x}RE_xFeO_3$

Fig. 4.1a shows X-ray diffraction diagram of $Bi_{1-x}Nd_xFeO_3$ (x = 0.00 ÷ 0.15). Crystal lattice parameters a, c, L_{XRD}, and c/a decrease when contcentration of Nd^{3+} increases (Fig. 4.2).

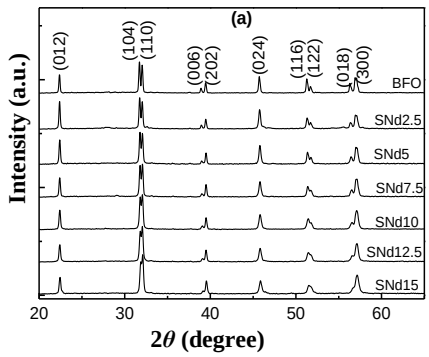

Fig. 4.1a. X-ray diffraction diagram of SNd system

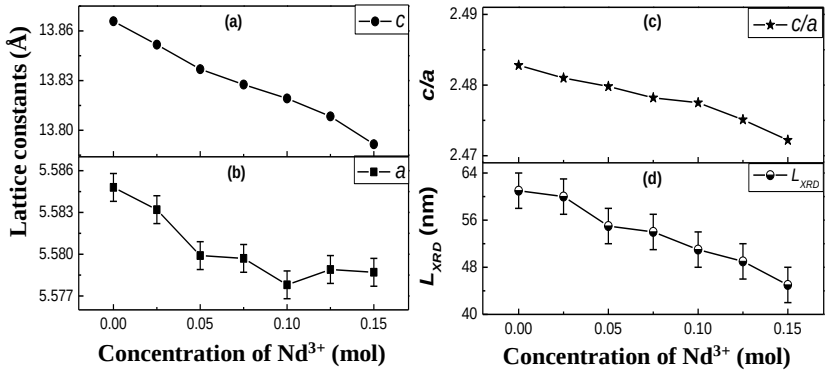

Fig. 4.2. The lattice parameters change versus concentration of Nd^{3+} (a) c; (b) a; (c) ratio c/a; (d) L_{XRD}

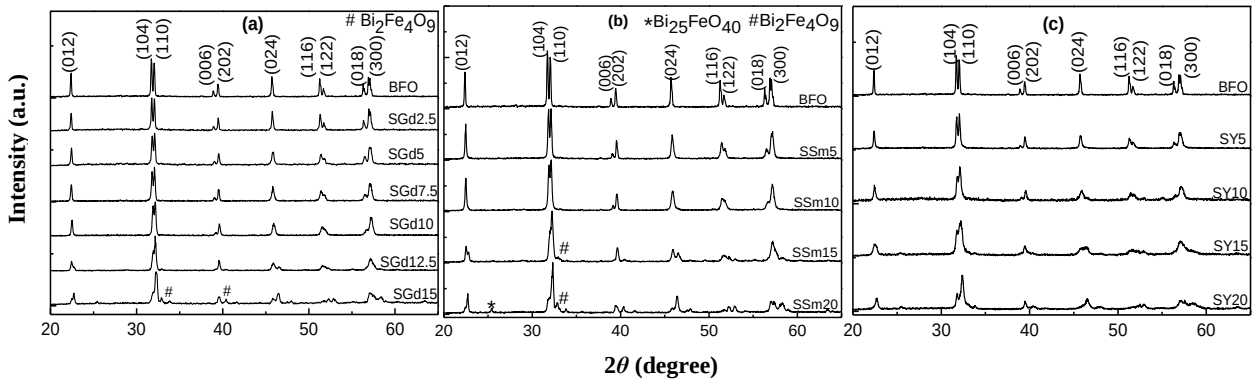

Fig. 4.3. X-ray diffraction diagram of doped systems: (a) SGd, (b) SSm, and (c) SY

To determine effects of rare-earth ionics on crystal structure of $BiFeO_3$, all samples were fabricated, conditions measured, and analysis method the same. X-ray diffraction diagram of samples of SGd, SSm, and SY systems were showed in Fig. 4.3. Crystal lattice constants and crystal grain size of these systems depend on concentration of dopants as showed in Fig. 4.4.

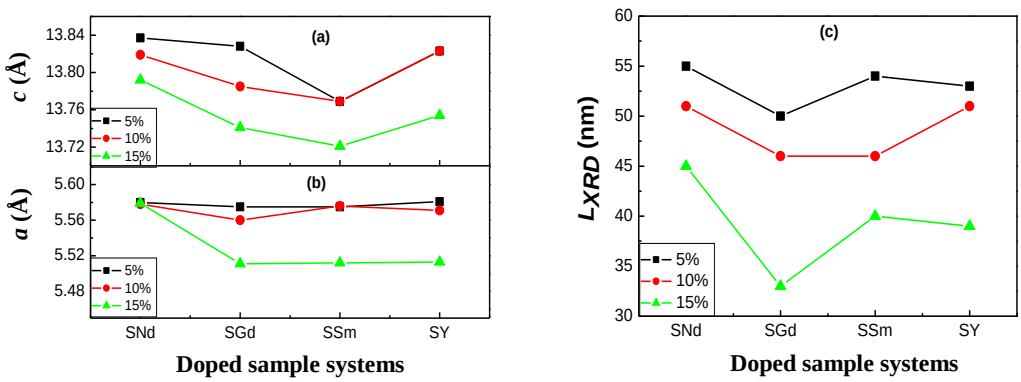

Fig. 4.4. (a, b) The lattice constants and (c) The crystals particle size with different doping concentration

In all three systems, we obverved that doping concentration was low (< 15 mol%) the samples have rhombohedral structure. When doping concentration was 15 mol% as in SGd and SSm systems, and 20 mol% in SY system, crystal structure of these samples change from rhomboheral structure to orthorhombic structure.

We can used Goldschmid factor (*t*) to determine the perovskite lattice distortion $BiFeO_3$ based on radius of ionic. Goldschmid factor of rare-earth ionics doped $BiFeO_3$ with different doping concentrations were showed in Fig. 4.7a. As such, the factor *t* reduced the most strongly vs. SY system, and that reduced the most lowly vs. SNd system. According to Goldschmid' theory, SY system has highest ratio *c/a*, SNd system has ratio *c/a* lowest. The experimental results of our compliance vs. Goldschmid's theory. Fig. 4.7b shows the changing of Goldschmid factor *t* and ratio *c/a* of rare-earth ionics doped $BiFeO_3$ vs. doping concentration was 10 mol%.

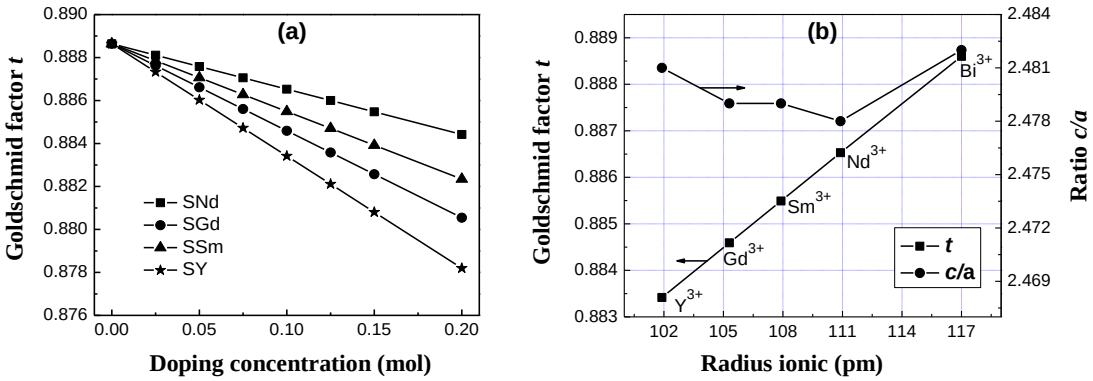

Fig. 4.7. (a) Goldschmid factor t of SNd, SGd, SSm, and SY systems; (b) Goldschmid factor t and ratio c/a of rare-earth ionic doped $BiFeO_3$ samples with doping concentration 10 mol%

Fig. 4.8 and Fig. 4.9 are EDS spectra of samples in SNd and SGd systems. EDS spectra of $BieFO_3$ confirms only three elements of Bi, Fe and O, without presence of other elements. EDS spectra of SNd5, SNd10 and SNd15 samples of SNd system have peaks which characterize for Bi, Fe, O elements and two other peaks characterize for Nd element at position 5.23 and 5.75 keV. The EDS spectra of SGd5, SGd10 and SGd15 of SGd system are showed in Fig 4.9. We observed some peaks characterizing for Bi, Fe, O elements and four peaks characterizing for Gd element at position 1.17, 1.88, 6.03, and 6.72 keV.

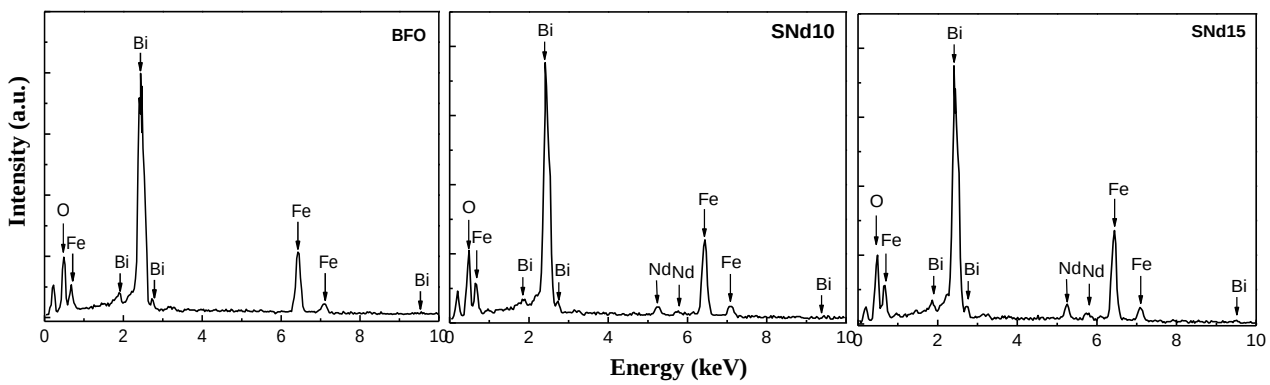

Fig. 4.8. EDS spectra of BFO, SNd5, SNd10 and SNd15 samples

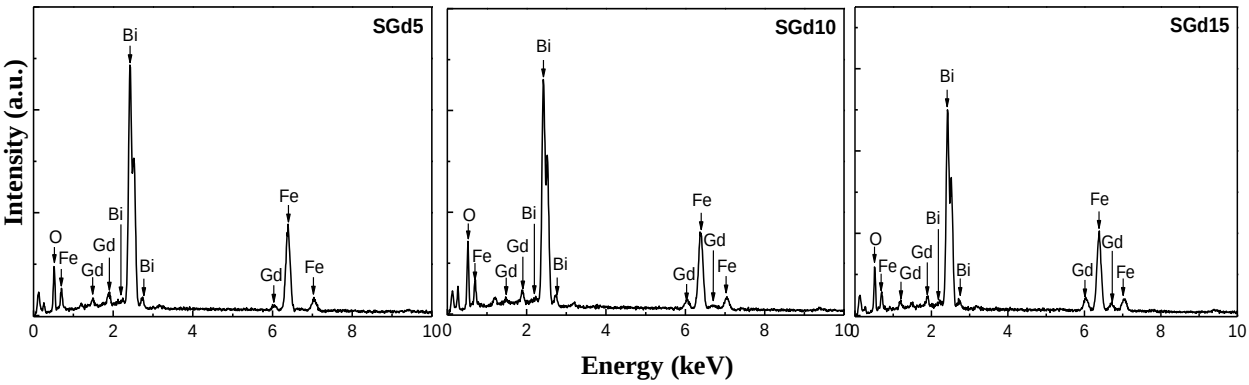

Fig. 4.9. EDS spectra of SGd5, SGd10 and SGd15

4.1.2. Crystal lattice vibrations of $Bi_{1-x}RE_xFeO_3$

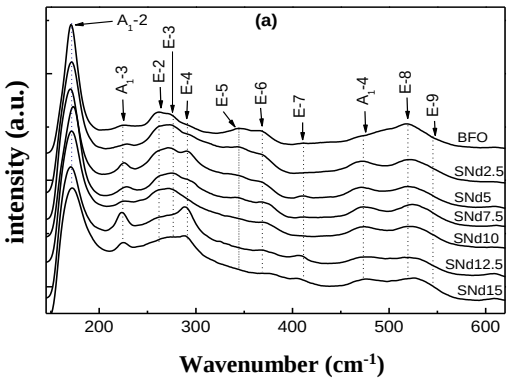

Fig. 4.10a. Raman scattering spectra of SNd system

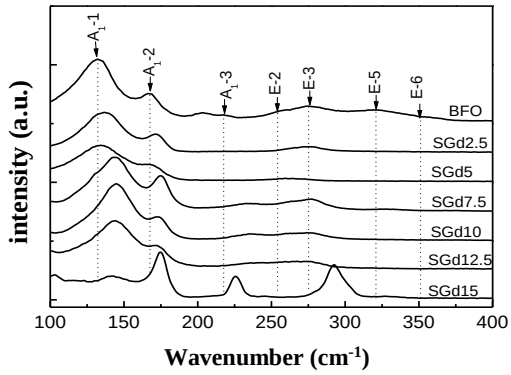

Fig. 4.11. Raman scattering spectra of SGd system

Fig. 4.10a shows Raman scattering spectra of the samples of SNd system. The modes A_1-2, *E*-2, *E*-3 which characterized for Bi-O bonding showed a shift toward higher wavenumber side and these peaks were expanded when the concentration of Nd^{3+} increased. For Gd^{3+}doped $BiFeO_3$, Raman scattering spectra of the samples of SGd system were also similar to those Raman scattering spectra results of the samples of SNd system (Fig. 4.11). When concentration of Gd^{3+} increased to 15 mol%, the intensity of peaks A_1-1 and A_1-2 were reduced, while the intensity of peaks A_1-3 and *E*-4 were enhanced and shifted towards higher wavenumber. These results combined with results of XRD diagram showed a sign of crystal structure transfer from rhombohedral structure to orthorhombic structure when the concentration of Gd^{3+} increased to 15 mol%.

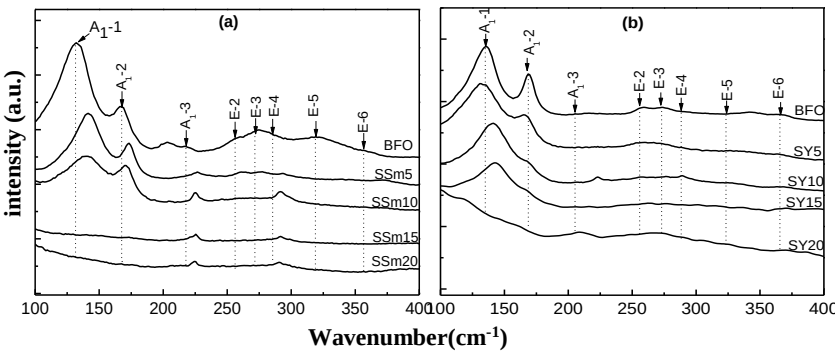

Fig. 4.12. Raman scattering spectra (a) SSm and (b) SY systems

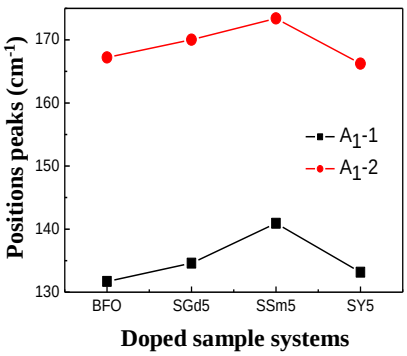

Fig. 4.13. Positions of peaks A_1-1, A_1-2

Raman scattering spectra of SSm and SY systems were represented in Fig. 4.12. In both SSm and SY systems, we could observed that those peaks which characterize for Bi - O bonding were

shiftted towards higher wavenumber when doping concentration was low (< 15 mol% for SSm system; < 20 mol% for SY system). Doping concentration was high (≥ 15 mol% for SSm system; ≥ 20 mol% for SY system), the intensity of some peaks decreased sharply, some peaks even disappeared. The positions of peaks A_1-1 and A_1-2 of BFO, SGd5, SSm5 and SY5 samples were showed in Fig. 4.13.

4.1.3. Surface morphology of rare-earth ionics doped $BiFeO_3$

Surface morphology and particle size of $BiFeO_3$ were determined by scanning electron micrographs (SEM) and transmission electron micrographs (TEM). From TEM image showed that $BiFeO_3$ crystalline had hexagonal shaped with grain size about 50 ÷ 70 nm. The grain size determined from TEM images was matched to the crystal particle size determined from data of XRD measurements. SEM images of the samples of SNd systems showed that the surface morphology of the samples was not uniform and agglomerate of particles. For SNd2.5, SNd7.5 and SNd5 samples, particles tended to grow along one direction and formed rod-shaped geometries. The remaining samples of SNd system seeds fake form bridges, grain boundaries were not clear and particle sizes tend to decreased when the concentration of Nd^{3+} increased.

4.2. Physical properties of $Bi_{1-x}RE_xFeO_3$ (*RE* = Nd, Gd, Sm, Y)

4.2.1. Optical properties of $Bi_{1-x}RE_xFeO_3$

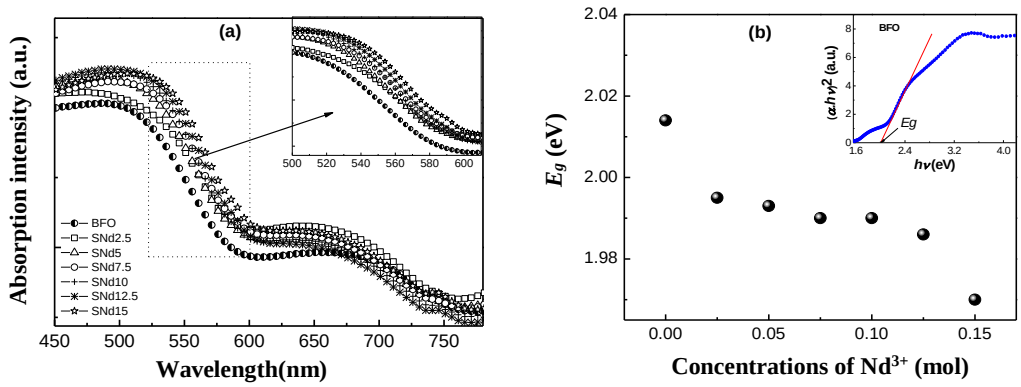

Fig. 4.16. (a) Absorption spectroscopy and (b) E_g change versus concentration of Nd^{3+}

Absorption spectroscopy of the samples of SNd system are showed in Fig. 4.16a. We observed two absorption bands at wavelength about 500 ÷ 600 nm and 650 ÷ 730 nm. Moreover, the absorption spectroscopy of SNd10, SNd12.5, and SNd15 samples, there is a small absorption peak at wavelength 750 nm. Fig. 4.16b shows the band gap values (E_g) change versus the concentrations of Nd^{3+}. Absorption spectroscopy of SGd, SSm, and SY systems are similar to those of SNd system, they have two absorption bands at wavelength 500 ÷ 600 nm and 650 ÷ 730 nm. The band gap values of SGd, SSm, and SY systems change versus the doping concentration are showed in Fig. 4.17b, Fig. 4.18b, and Fig. 4.19b.

Optical absorption spectroscopy of rare-earth ionics (Nd^{3+}, Gd^{3+}, Sm^{3+} and Y^{3+}) doped $BiFeO_3$ have common features, i.e, the shift toward higher wavelength of absorption edge, peak absorption and leg absorption edge, and the decreasing of effective band gap values when doping concentrations increase. Energy band structure of $BiFeO_3$ material was altered results in the formation of impurity lead to energy levels with in the energy band gap, which caused the reducing optical band gap of the materials.

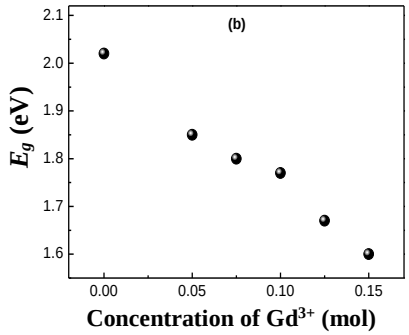

Fig. 4.17b. E_g change versus the concentration of Gd^{3+}

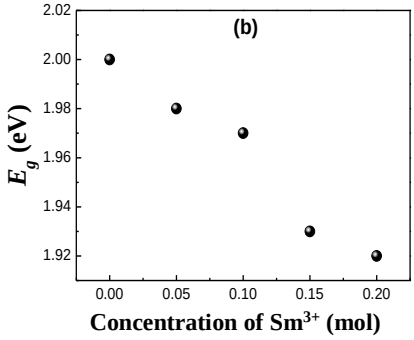

Fig. 4.18b. E_g change versus the concentration of Sm^{3+}

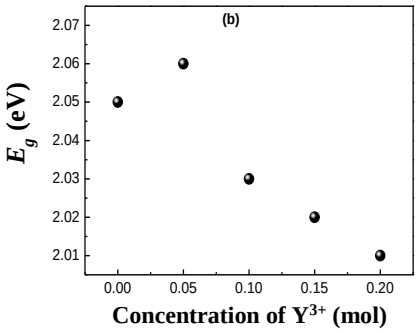

Fig. 4.19b. E_g change versus the concentration of Y^{3+}

4.2.2. Magnetic properties of $Bi_{1-x}RE_xFeO_3$

In this section, we present the effects of rare-earth ionics to magnetic properties of $BiFeO_3$. Fig. 4.20 shows magnetic hysteresis loops of $Bi_{1-x}Nd_xFeO_3$. The change of *Ms* and *Mr* values versus the concentration of Nd^{3+} are showed in Fig. 4.21. Results show that *Ms* and *Mr* values increase with the increasing of Nd^{3+} concentration.

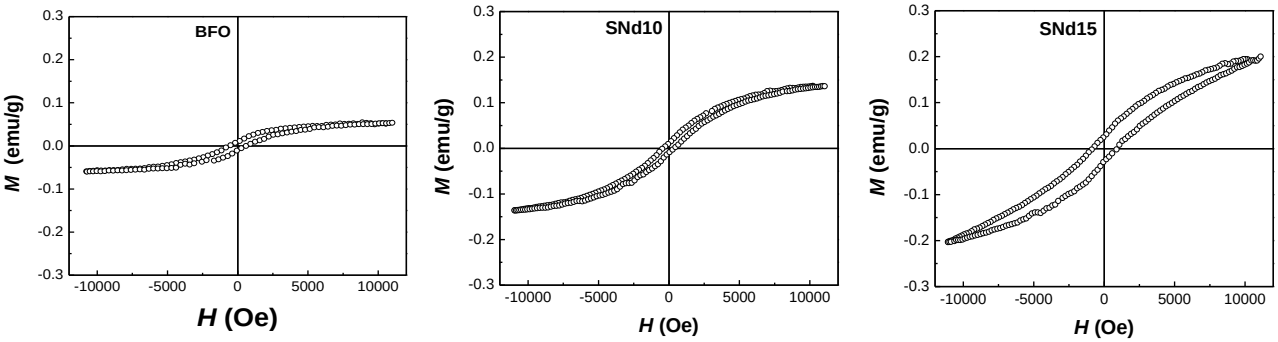

Fig. 4.20. Magnetic hysteresis loops of $Bi_{1-x}Nd_xFeO_3$

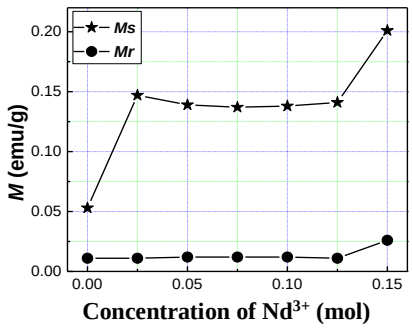

Fig. 4.21. Ms and Mr change versus concentrantion of Nd^{3+}

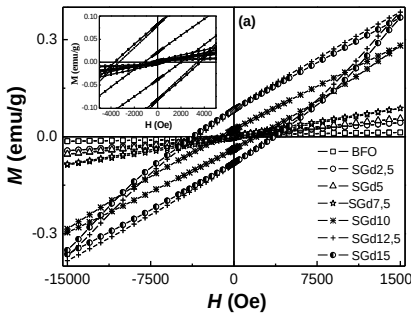

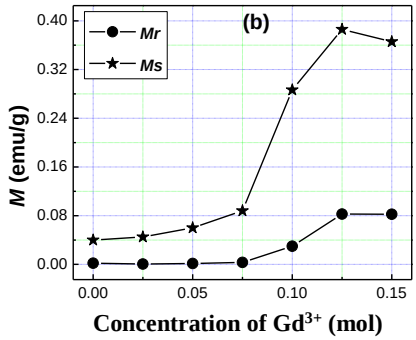

Fig. 4.22. (a) Magnetic hysteresis loops of SGd systems; (b) Ms and Mr change versus concentration of Gd^{3+}

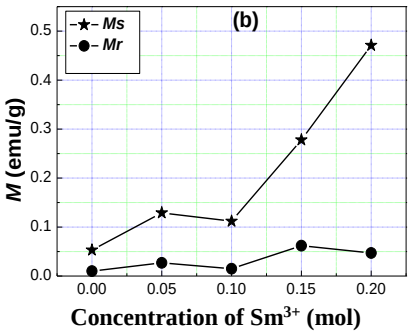

Fig. 4.23b. Ms and Mr change versus concentration of Sm^{3+}

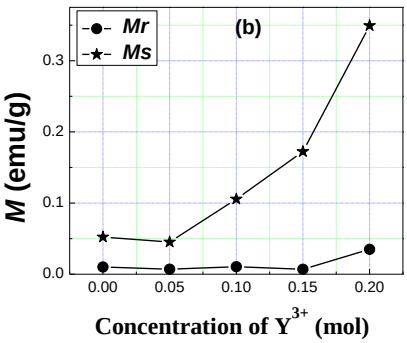

Fig. 4.24b. Ms and Mr change versus concentration of Y^{3+}

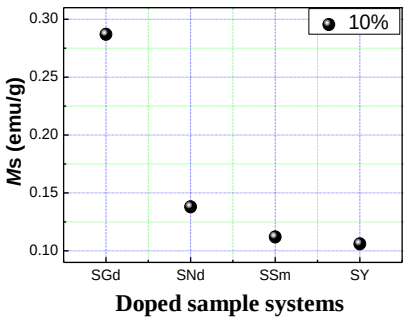

Fig. 4.25. Ms value of SNd, SSm and SY systems with doping concnetration is 10 mol%

Fig. 4.22a shows magnetic hysteresis loops of the samples of SGd systems. We noticed that magnetic hysteresis loops of SGd10, SGd12.5, and SGd15 samples have not reached the saturated value. In addition, the change of *Ms* and *Mr* versus the concentration of Gd^{3+} are showed in Fig. 4.22b. All *Ms* and *Mr* values increase when the concentration of Gd^{3+} increase. Similar to SNd and SGd systems, magnetic hysteresis loops of the samples of SSm and SY systems show that all samples possesed weak ferromagnetic order. *Ms* and *Mr* values of the samples of SSm and SY systems change versus the doping concentration are showed in Fig. 4.23b and Fig. 4.24b.

To compare the effects of different rare-earth ionics to magnetic properties of $BiFeO_3$, we analyzed the magnetic hysteresis loops of SNd, SSm, SY systems with doping concentrations was 10 mol%, and *Ms* values of samples are showed in Fig. 4.25.

4.2.3. Electrical properties of $Bi_{1-x}RE_xFeO_3$

Effect of rare-earth ionics to electrical properties of $BiFeO_3$ materials as follows: (i) impedance spectra of rare-earth ionics doped $BiFeO_3$ with doping concentrations is low, contribute to impedance spectra are grain and grain boundaries. When the doping concentration is high, contributing to impedance spectra only grain; (ii) rare-earth ionics doped $BiFeO_3$ effect on crystal structure of materials leading to effect electrical properties of these materials.

4.2.4. Ferroelectric properties of Gd^{3+}doped $BiFeO_3$

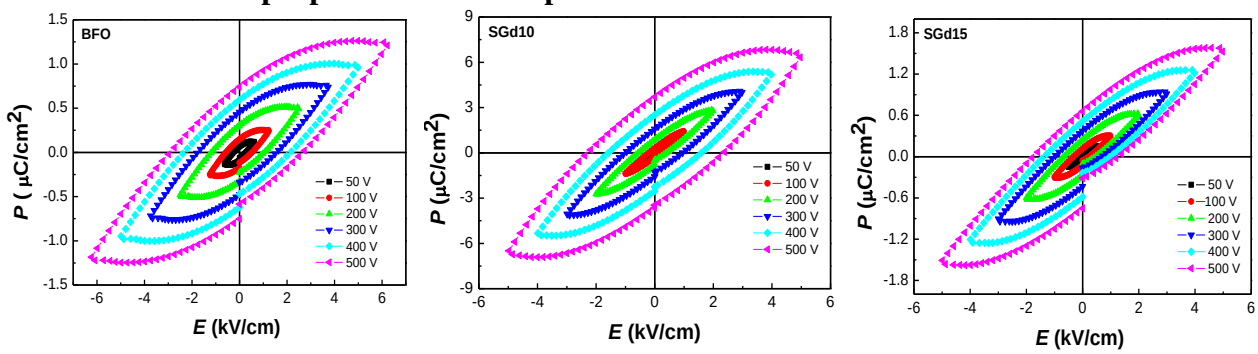

Fig. 4.29. Polarization hysteresis (P-E) loops of BFO; SGd10, and SGd15 samples

Fig. 4.29 shows polarization hysteresis loops of SGd systems measured at room temperature. $BiFeO_3$ had $Ps = 0.129 \div 1.260$ μC/cm^2, $Pr = 0.083 \div 0.749$ μC/cm^2, and $\varepsilon = 228$. *Ps*, *Pr* and ε values change versus the concentration of Gd^{3+} are showed in Fig. 4.30. We noticed that *Ps*, *Pr*, ε and *J* values increase when concentration of Gd^{3+} increases from 0 to 10 mol% then that of reduce when concentration of Gd^{3+} increases to 15 mol%. Moreover, leakage current density of $BiFeO_3$ is $5.249.10^{-4}$ A/cm^2. Gd^{3+} doped $BiFeO_3$ leads to reduces the leakage current density of material. The leakage current density value is the smallest as the concentration of Gd^{3+} is 10 mol% (Fig. 4.30c).

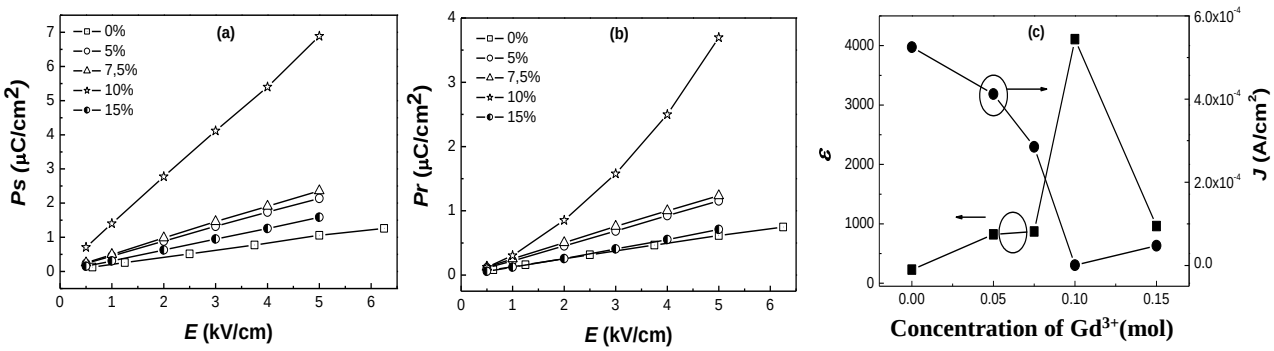

Fig. 4.30. Ps, Pr, ε, and J change versus concentration of Gd^{3+}: (a) Ps; (b) Pr; (c) ε and J

Chapter 5: CRYSTAL STRUCTURE, PHYSICAL PROPERTIES OF RARE-EARTH AND TRANSITION METAL IONS CO-DOPED $BiFeO_3$

5.1. Crystal structure, crystal lattice vibrations and surface morphology of $Bi_{1-x}RE_xFe_{0.975}Ni_{0.025}O_3$(*RE*= Nd, Gd; *x* = 0.00 ÷ 0.15)

5.1.1. Crystal structure of $Bi_{1-x}RE_xFe_{0.975}Ni_{0.025}O_3$

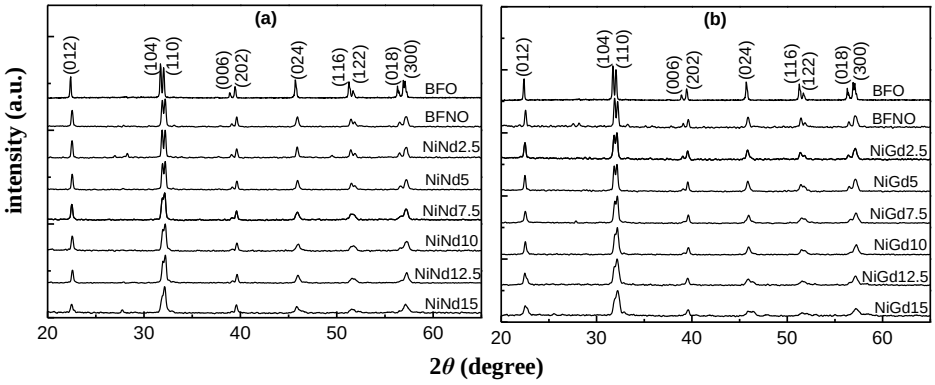

Fig. 5.1. X-ray diffraction diagram of rare-earth and transition metal ionics co-doped $BiFeO_3$ (a) SNiNd and (b) SNiGd systems

Fig. 5.1 shows X-ray diffraction diagram of $Bi_{1-x}RE_xFe_{0.975}Ni_{0.025}O_3$ (*RE* = Nd, Gd; *x* = 0.00 ÷ 0.15). In both SNiNd and SNiGd systems, crystal lattice parameters *a*, *c*, L_{XRD}, and *c/a* decrease when contcentration of rare-earth ionics increase (Fig. 5.2). Moreover, XRD diagram of NiNd15 and NiGd15 samples showed peaks (104) and (110) tends to peak superposition into a single, peak (024) tend to split into two peaks. This is a sign that there was a structural phase transition when doping concentration increases to 15 mol%.

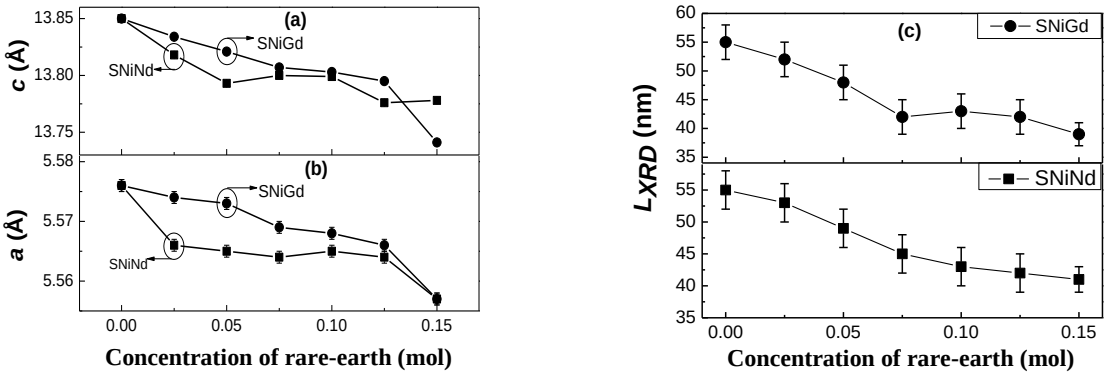

Fig. 5.2. The lattice parameters of SNiNd and SNiGd systems change versus doping concentration (a) Constant a; (b) Constant c; (c) Crystals particle size L_{XRD}

To observe the effects of Nd^{3+} and Ni^{2+} co-doped $BiFeO_3$ on crystal structure. We surveyed X-ray diffraction diagram of 10 mol% Nd^{3+} and 5 mol% Ni^{2+} co-doped $BiFeO_3$ (BNFNO) and compared with those of BFO, SNd10, and NiNd10 samples (Fig. 5.3a). Fig. 5.3b shows crystal lattice constants, and crystals particle size of BFO, SNd10, NiNd10 and BNFNO samples. The effect of impurity on crystal structure in (Nd^{3+}, Ni^{2+}) co-doped samples was higher than that of in Nd^{3+} doped samples. The level of effect increased with increasing concentration of Ni^{2+}.

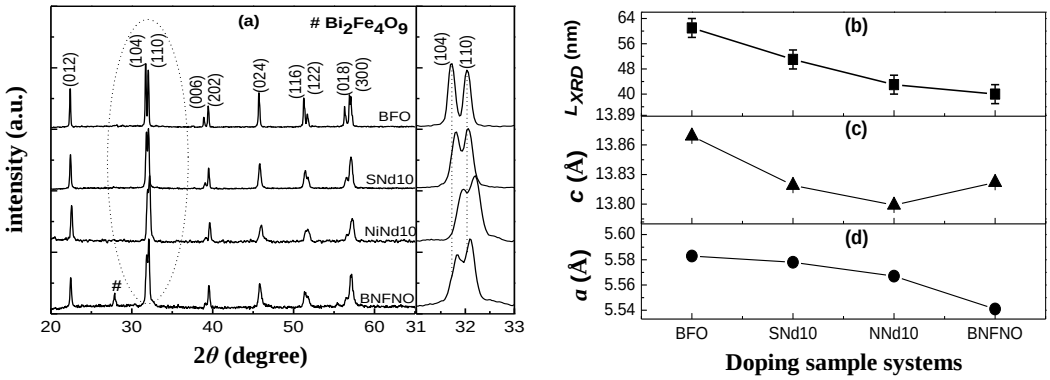

Fig. 5.3. (a) X-ray diffraction diagram; (b) Crystals grain size L_{XRD}; (c) Constant a; (d) Constant c of BFO, SNd10, NiNd10 and BNFNO samples

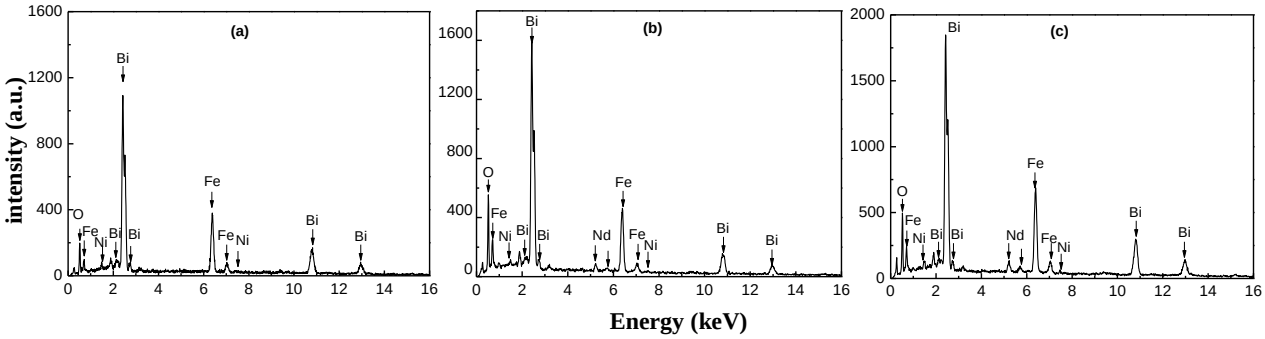

Fig. 5.4. EDS spectra of SNiNd system: (a) BFNO; (b) NiNd5 and (c) NiNd10

Fig. 5.4 shows EDS spectra of BNFNO, NiNd5, NiNd10 and NiNd15 samples. EDS spectra of BFNO sample confirmed only four elements of Bi, Fe, O and Ni, without presence of other elements. EDS spectra of NiNd5, NiNd10 and NiNd15 samples had peaks which are characterized for Bi, Fe, O, Ni elements and two peaks characterizing for Nd element were at position 5.20 and 5.73 keV. Intensity of these peaks increased when concentration of Nd^{3+} increased. Fig. 5.5 shows EDS spectra of NiGd5, NiGd10 and NiGd15 samples. In these systems, the peaks characterizing of Bi, Fe, O and Ni elements were at the same position as those in the SNiNd system. EDS spectra of these samples also had characteristic peaks of Gd at position 1.22 and 6.03 keV.

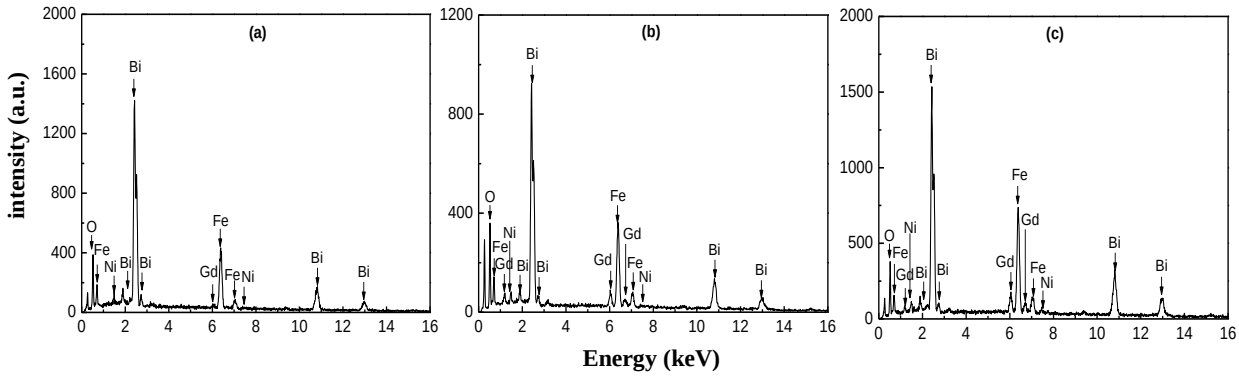

Fig. 5.5. EDS spectra of SNiGd system: (a) NiGd5; (b) NiGd10 and (c) NiGd15

5.1.2. Crystal lattice vibrations of $Bi_{1-x}RE_xFe_{0.975}Ni_{0.025}O_3$

Fig.5.6 shows Raman scattering spectra of SNiNd and SNiGd systems. Raman scattering spectra of $BiFeO_3$ at wavenumber 100 ÷ 400 cm^{-1} have 9 modes at 130,167, 205, 219, 261, 277, 289, 323, and 358 cm^{-1} corresponding to modes A_1-1, A_1-2, A_1-3, E-2, E-3, E-4, E-5, E-6. For rare-earth and Ni^{2+} ionics co-doped samples, intensity of these modes decrease sharply. The mode A_1-1 of

BFNO sample shifts towards lower wavenumber. The mode A_1-1 of (Nd^{3+}, Ni^{2+}) co-doped $BiFeO_3$ tend to shift towards higher wavenumber. This change is due to the substitution of Nd^{3+} into Bi^{3+}, which leads to the change of both number Bi - O bonding and length Bi – O bonding. Fig. 5.6b shows Raman scattering spectra of SNiGd system which is similar to that of SNiNd system. Intensity of Raman peaks decrease sharply when (Gd^{3+}, Ni^{2+}) co-doped $BiFeO_3$. For (Nd^{3+}, Ni^{2+}) co-doped $BiFeO_3$, modes A_1-1, A_1-2 tend to shift toward higher wavenumber when the contentration of Nd^{3+} increases (Fig. 5.7a). For (Gd^{3+}, Ni^{2+}) co-doped $BiFeO_3$, modes A_1-1, A_1-2 tend to shift toward higher wavenumber when the contentration of Gd^{3+} increases from 0 to 10 mol%. When the concentration of Gd^{3+} is higher than 10 mol%, Raman modes are extinguished (Fig. 5.7b).

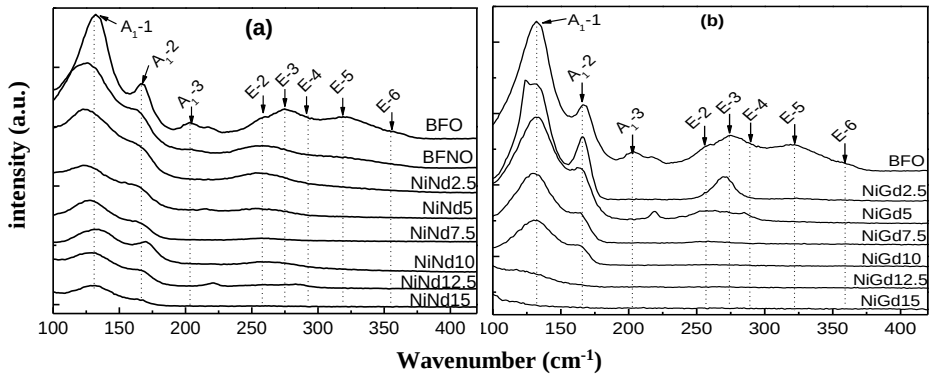

Fig. 5.6. Raman scattering spectra of rare-earth and Ni^{2+}ionics co-doped $BiFeO_3$ (a) SNiNd and (b) SNiGd systems

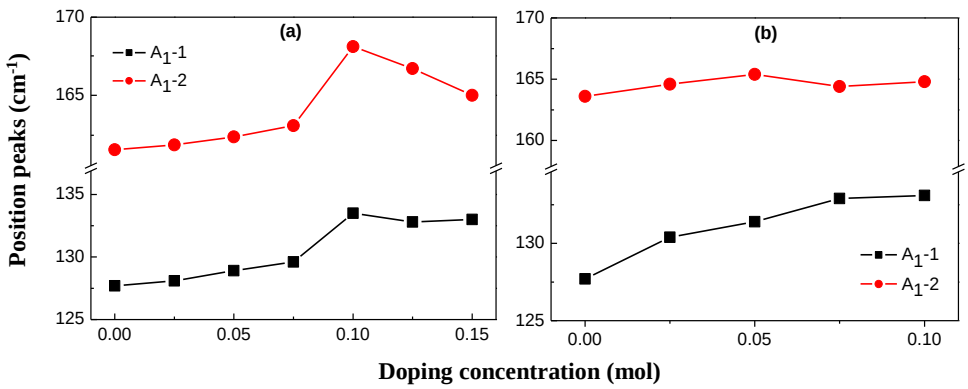

Fig. 5.7. Position peaks A_1-1, A_1-2 change versus doping concentration (a) SNiNd and (b) SNiGd systems

5.1.3. Scanning electron microscope images of $Bi_{1-x}RE_xFe_{0.975}Ni_{0.025}O_3$

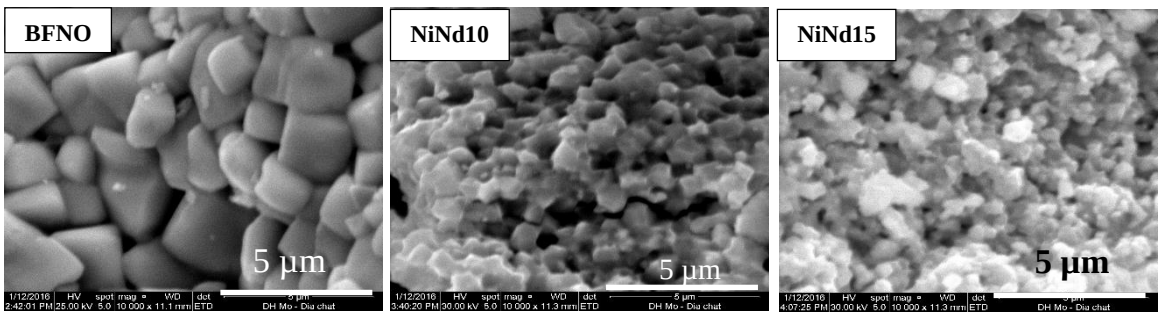

Fig. 5.8. SEM images of samples of SNiNd system

SEM images of the samples of SNiNd and SNiGd systems are showed in Fig. 5.8 and Fig. 5.9, respectively. SEM images of the samples of SNiNd system indicated that these samples have fairly

uniform particle size and surface morphology. Particle size of Ni^{2+} doped sample (BFNO) is about 2 µm. For rare-earth and Ni^{2+} ionics co-doped samples, particle size decreases when the concentration of Nd^{3+} increases. SEM images of samples of SNiGd system shows that particle size and surface morphology are less uniform than that of SNiNd system.

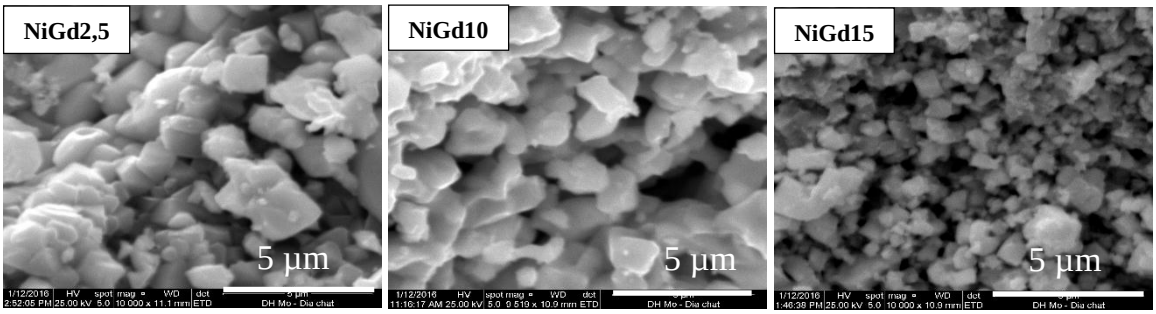

Fig. 5.9. SEM images of samples of SNiGd system

5.2. Physical properties of $Bi_{1-x}RE_xFe_{0.975}Ni_{0.025}O_3$ (*RE* = Nd, Gd)

5.2.1. Optical properties $Bi_{1-x}RE_xFe_{0.975}Ni_{0.025}O_3$

Fig. 5.10 shows absorption spectroscopy of SNiNd and SNiGd systems. When that compared to absorption spectroscopy of $BiFeO_3$, we obsreved the absorption edge, peak absorption, and leg absorption edge of (Nd^{3+}, Ni^{2+}) or (Gd^{3+}, Ni^{2+}) co-doped samples shift towards higher wavelength when the concentration of Nd^{3+} (or Gd^{3+}) increases.

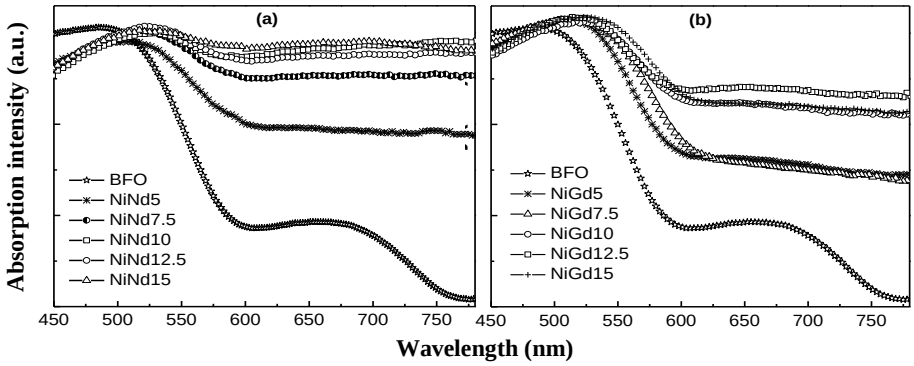

Fig. 5.10. Absorption spectroscopy of SNiNd and SNiGd systems: (a) SNiNd; (b) SNiGd

5.2.2. Magnetic properties of $Bi_{1-x}RE_xFe_{0.975}Ni_{0.025}O_3$

Magnetic hysteresis loops of SNiNd and SNiGd systems are measured at room temperature with magnetic field about 10 kOe (Fig. 5.11a and Fig. 5.12a).

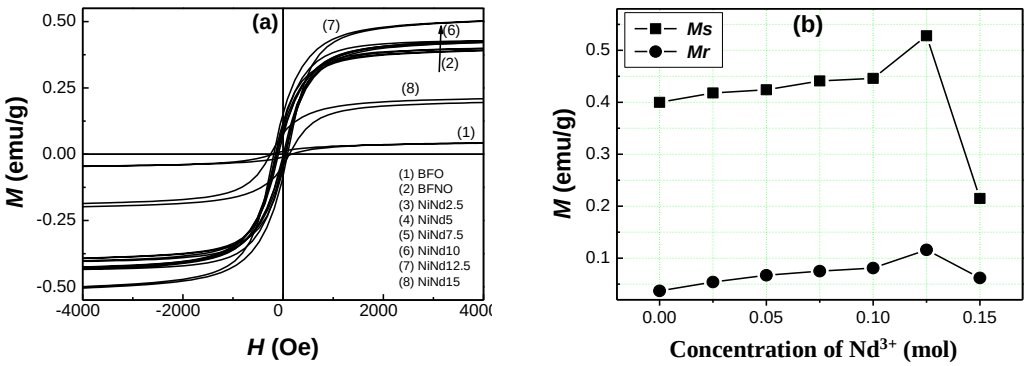

Fig. 5.11. (a) Magnetic hysteresis loops of SNiNd system and (b) Ms and Mr change versus concentration of Nd^{3+}

Experimental results showed that $BiFeO_3$ was weak ferromagnetic order with *Ms* = 0.053 emu/g, and *Mr* = 0.011 emu/g. The co-doping of rare-earth and Ni^{2+} $BiFeO_3$ leads to sharply increasing of *Ms* and *Mr*. Moreover, in both SNiGd and SNiNd systems, *Ms* and *Mr* values increases as concentration of Nd^{3+} (or Gd^{3+}) increases from 0 to 15 mol%. The *Ms* and *Mr* values are the highest when the doping concentration increases to 12.5 mol% (Fig. 5.11b and Fig. 5.12b).

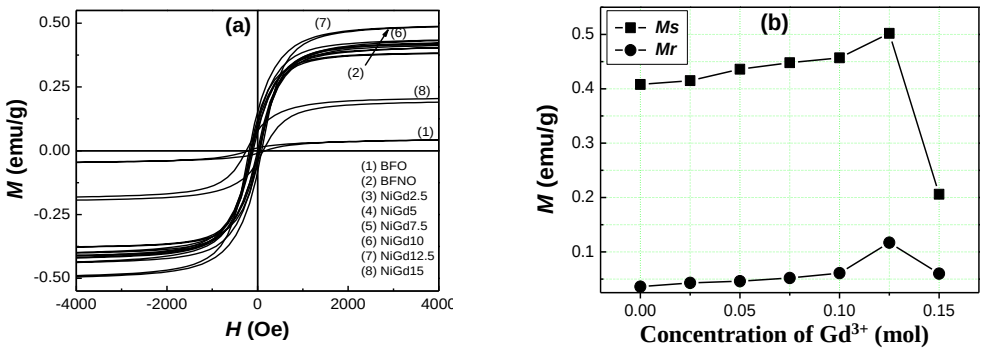

Fig. 5.12. (a) Magnetic hysteresis loops of SNiGd system and (b) Ms and Mr change versus concentration of Gd^{3+}

In order to observe effects of Nd^{3+} and Ni^{2+} ionics co-doped $BiFeO_3$ to magnetic properties of this material, we measured magnetic hysteresis loops of 10 mol% Nd^{3+} and 5 mol% Ni^{2+} co-doped $BiFeO_3$ (BNFNO) and compared with magnetic hysteresis loops of BFO, SNd10, and NiNd10 samples. Fig.5.13 shows magnetic hysteresis loops and *Ms*, *Mr* values of BFO, SNd10, NiNd10, and BNFNO samples. *Ms* and *Mr* values of BFO, SNd10, NNd10, and BNFNO samples are *Ms* = 0.053, 0.138, 0.443, and 1.969 emu/g and *Mr* = 0.011, 0.012, 0.061, and 0.301 emu/g, respectively.

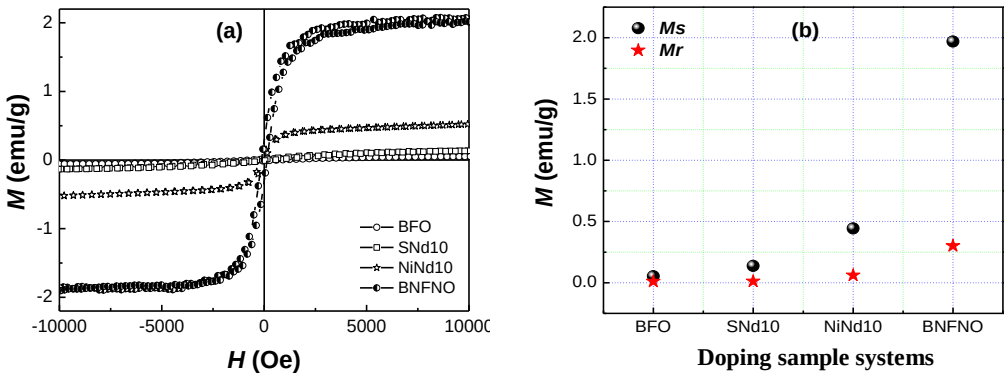

Fig. 5.13. (a) Magnetic hysteresis loops (b) Ms, Mr values of BFO, SNd10, NNd10, and BNFNO samples

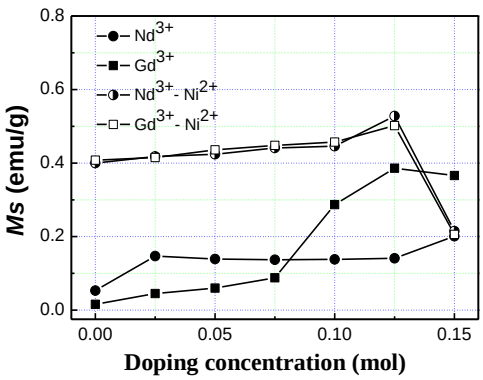

Fig. 5.14. Ms of rare-earth ionics doped $BiFeO_3$ and co-doped $BiFeO_3$

The comparision of *Ms* of co-doped samples and rare-earth doped samples at different doping concentrationis are showed in Fig. 5.14. Results show that the ferromagnetic properties of co-doped samples are improved more than that of rare-earth doped samples.

5.2.3. Ferroelectric properties of $Bi_{1-x}RE_xFe_{0.975}Ni_{0.025}O_3$

In this section, we present effects of rare-earth and Ni^{2+} ionics co-doped $BiFeO_3$ on ferroelectric properties. Polarization hysteresis loops of SNiNd and SNiGd systems are showed in Fig. 5.15 and Fig. 5.17, respectively.

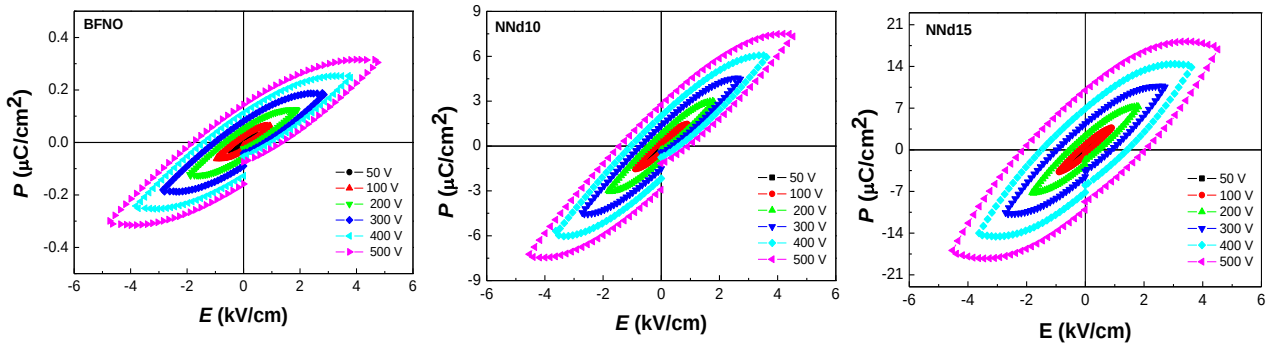

Fig. 5.15. Polarization hysteresis (P-E) loops of samples of SNiNd system

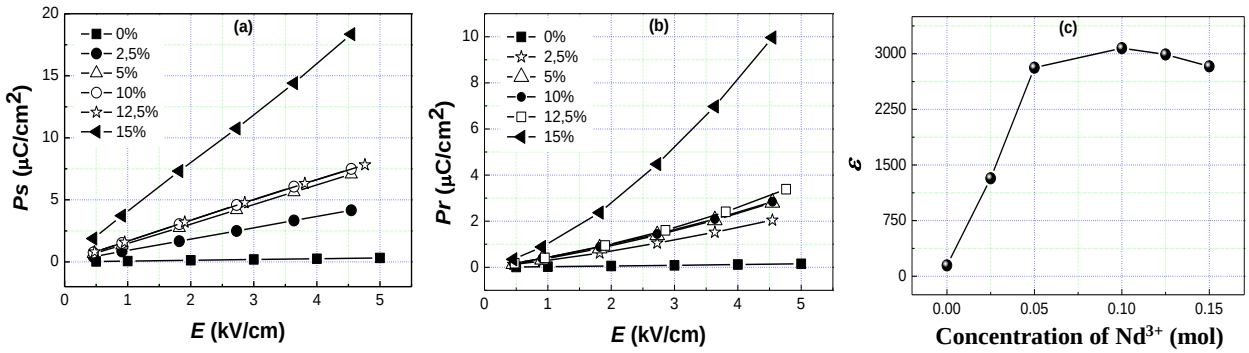

Fig. 5.16. Ps, Pr, and ε of SNiNd system change versus concentration of Nd^{3+} (a) Ps; (b) Pr; and (c) ε

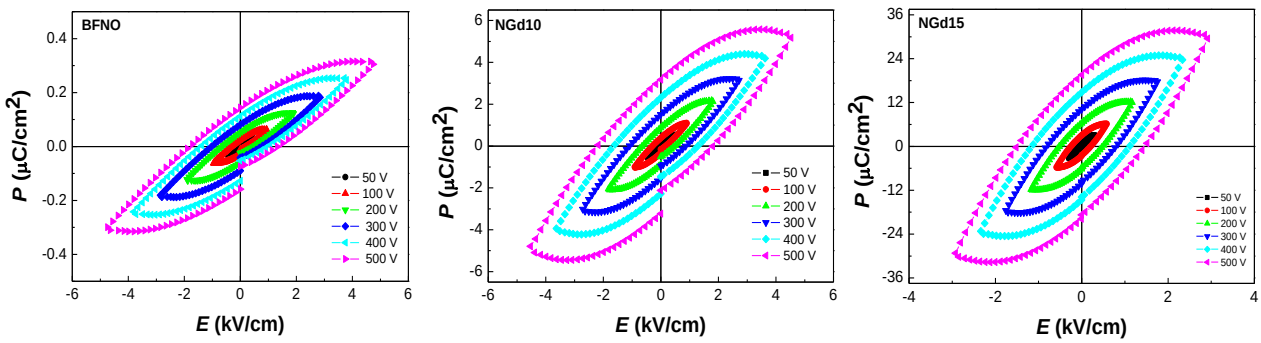

Fig. 5.17. Polarization hysteresis (P-E) loops of samples of SNiGd system

Ps, *Pr*, and ε values change versus impurity concentration are showed in Fig. 5.16 and Fig. 5.18, respectively. Co-doping of (Nd^{3+}, Ni^{2+}) or (Gd^{3+}, Ni^{2+}) $BiFeO_3$, the ferromagnetic and ferroelectric properties of these materials have been improved. It suggests that multiferroic properties of $BiFeO_3$ have been improved by co-doping of (Nd^{3+}, Ni^{2+}) or (Gd^{3+}, Ni^{2+}). In the concentration ranges of Nd^{3+} (or Gd^{3+}) from 0 to 15 mol%, the best improvement of multiferroic properties is achieved at 12.5 mol% Nd^{3+} (or Gd^{3+}) and 2.5 mol% N^{2+}.

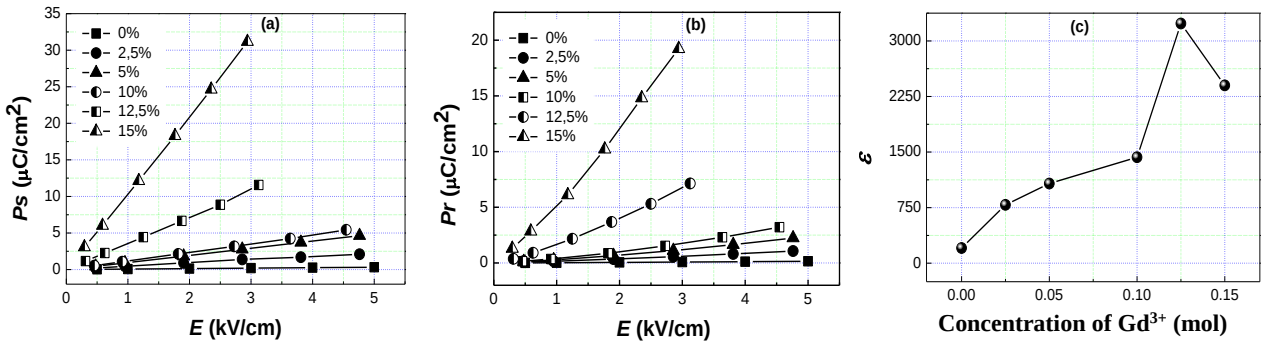

Fig. 5.18. Ps, Pr, ε values of NGd system change versus concentration of Gd^{3+} (a) Ps; (b) Pr and (c) ε

CONCLUSION

1. The bismuth ferrite ($BiFeO_3$) material was successfully synthesized by solid state reaction, hydrothermal and sol-gel methods. The single phase $BiFeO_3$ powders were obtained by the sol-gel method with the optimal condition of calcination at 800 °C for 7 hours. It was suitable for doping dopants into $BiFeO_3$.
2. A reduction of the band gap of $BiFeO_3$-based materials has been observed in the rare earth doped (Nd^{3+} or Gd^{3+}, Sm^{3+}, Y^{3+}) and co-doped (Nd^{3+} and Ni^{2+} or Gd^{3+} and Ni^{2+}) samples in comparison with that of the pristine one. The 2.02 eV band gap of the $BiFeO_3$ material can be reduced to 1.60 eV or 1.63 eV corresponding to $BiFeO_3$ materials doped with 15 mol% Gd^{3+} or co-doped with 15 mol% Nd^{3+} and 2.5 mol% Ni^{2+}.
3. At room temperature, pure $BiFeO_3$ showed a weak ferromagnetic order with *Ms* = 0.053 emu/g. The ferromagnetic properties of $BiFeO_3$ materials can be significantly improved by rare earth doped (Nd^{3+}, Gd^{3+}, Sm^{3+}, Y^{3+}) and co-doped (Nd^{3+} and Ni^{2+} or Gd^{3+} and Ni^{2+}) materials. The saturation magnetization value *(Ms)* of the Gd^{3+} doped or Gd^{3+} and Ni^{2+} co-doped $BiFeO_3$ materials can be increased 8.9 or 10 times higher than that of the pure $BiFeO_3$ one, respectively.
4. An enhancement of the ferroelectricity of pure $BiFeO_3$ is obtained for Gd^{3+} doped and Nd^{3+} and Ni^{2+} or Gd^{3+} and Ni^{2+} co-doped $BiFeO_3$ materials. The spontaneous electric polarization (*Ps*) and residual electric polarization *(Pr)* of the $BiFeO_3$ material are enhanced from *Ps* = 1.26 μC/cm^2, *Pr* = 0.75 μC/cm^2 up to *Ps* = 6.89 μC/cm^2, *Pr* = 3.70 μC/cm^2 for doping 10 mol% Gd^{3+}, and *Ps* = 31.17μC/cm^2, *Pr* = 19.22 μC/cm^2 for co-doping 15 mol% Gd^{3+} and 2.5 mol% Ni^{2+} into the pure $BiFeO_3$ material.

LIST OF PUBLICATIONS

1. Dao Viet Thang, Du Thi Xuan Thao, and Nguyen Van Minh(2016), "Magnetic properties and Impedance spectroscopic Studies of multiferroic $Bi_{1-x}Nd_xFeO_3$ materials", *J. Mag.*, 21(1), pp. 29-34.
2. Dao Viet Thang, Du Thi Xuan Thao, Ngo Thi Cam Linh, and Nguyen Van Minh (2016), "Effect of rare earths and transition metals co-doped on structural, optical and magnetic properties of $BiFeO_3$ materials", *J. Sci. Tech.*54 (1A), pp 96-103.
3. Dao Viet Thang, Du Thi Xuan Thao, Le Thi Mai Oanh, and Nguyen Van Minh (2015), "Effect of neodymium and transition metals co-doped on structural, optical and magnetic properties of $BiFeO_3$ materials", *J. Sci. VNU: Math.Phys.*31 (3), pp. 63-69.

4. Dao Viet Thang, Du Thi Xuan Thao, Tran Thi Thu Ha, and Nguyen Van Minh (2015), "Structural, and optical properties of Gd doped $BiFeO_3$ materials", *Tuyển tập báo cáo hội nghị Vật lí chất rắn và khoa học vật liệu toàn quốc lần thứ 9 (SPMS-2015), Quyển II*, tr. 735-738.
5. Dao Viet Thang, Du Thi Xuan Thao, Nguyen Van Minh (2014), "Effect of Nd-doping on structural, optical and magnetic properties in multiferroic $BiFeO_3$ materials", *J. Sci. Tech.*52 (3C), pp. 443-452.
6. Đào Việt Thắng, Hoàng Văn Tiến, Dư Thị Xuân Thảo, Lê Thị Mai Oanh, Đỗ Thu Hà và Nguyễn Văn Minh (2014), "Khảo sát ảnh hưởng điều kiện công nghệ lên cấu trúc, tính chất từ và quang học của vật liệu $BiFeO_3$", *J. Sci. HNUE* 59 (1A), tr. 3-8.
7. Đào Việt Thắng, Dư Thị Xuân Thảo, Nguyễn Thị Diệu Thu, Hồ Quỳnh Anh và Nguyễn Văn Minh (2014), "Nghiên cứu ảnh hưởng Nd lên tính chất của vật liệu $BiFeO_3$", *J. Sci. HNUE* 59 (1A), pp. 9-15.
8. Dao Viet Thang, Du Thi Xuan Thao, and Nguyen Van Minh (2014), "Structural, magnetic properties and complex impedance of multifrroic $BiFeO_3$ materials", *Proceedings of the second International Conference on Advanced Materials and Nanotechnology (ICAMN 2014),* pp. 32-37.
9. Đào Việt Thắng, Nguyễn Thị Minh Thu, Nguyễn Văn Minh (2014), "Chế tạo và nghiên cứu tính chất của vật liệu $BiFeO_3$ pha tạp Ni", *Tuyển tập báo cáo hội nghị những bộ trong Quang học, Quang phổ và Ứng dụng lần thứ 8,* tr. 755-760.
10. Dao Viet Thang, Du Thi Xuan Thao, and Nguyen Van Minh (2013), "Structral and physical properties of Y-doped $BiFeO_3$ material prepared by sol-gel method", *J. Sci. VNU: Math.-Phys.* 29 (3), pp. 63-69.
11. Dao Viet Thang, Nguyen Van Minh and Du Thi Xuan Thao (2012), "Study structural, optical and magnetic properties of $Bi_{0.85}M_{0.15}FeO_3$ (M = Sm, Y, Nd) materials", *Proceedings of International Conference on Advanced Materials and Nanotechnology (ICAMN),* pp. 192-195.
12. Nguyen Van Minh and Dao Viet Thang (2010), "Multiferroic materials $Bi_{1-x}Sm_xFeO_3$: A study of Raman and absorption spectroscopies", *J. Nonlinear Opt. Phys.* 19, pp. 247-254.
13. Nguyen Van Minh and Dao Viet Thang (2010), "Dopant effects on the structural, optical and electromagnetic properties in multiferroic $Bi_{1-x}Y_xFeO_3$ ceramics", *J. Alloys Compd.* 505, pp. 619-622.
14. Du Thi Xuan Thao, Dao Viet Thang, and Nguyen Van Minh, "Study of multiferroics $BiFeO_3$ materials: Structural, electrical and magnetic properties", *Proceedings of the 2nd International Conference on Scientific Research Cooperation between Vietnam and Poland in Earth Sciences (VIET-POL-2015),* pp. 395-400.
15. Dao Viet Thang, Nguyen Van Minh and Du Thi Xuan Thao (2012), "Study structural, optical and magnetic properties of Sm-doped $BiFeO_3$ multiferroics prepared by sol - gel method", *Proceedings of the 7th International Conference on Photonics and Applications (ICPA-7): Advances in Optics, Photonics, Spectroscopy & Applications VII,* pp. 300-304.
16. Đào Việt Thắng, Dương Anh Tuấn, Nguyễn Văn Quảng và Nguyễn Văn Minh (2010), "Chế tạo vật liệu multiferroic $BiFeO_3$ pha Nd và khảo sát đặc trưng của chúng", *Tuyển tập báo cáo Những tiến bộ trong Quang học, Quang phổ và Ứng dụng lần thứ 6,* tr. 729-733.